

Evidences of localized CO₂-induced diagenesis in the Cretaceous Quantou Formation, southern Songliao Basin, China



Kelai Xi ^{a,c,*}, Yingchang Cao ^{a,b,*}, Rukai Zhu ^d, Beyene Girma Haile ^c, Helge Hellevang ^{c,e,**}

^a School of Geosciences, China University of Petroleum, Qingdao, Shandong 266580, China

^b Laboratory for Marine Mineral Resources, Qingdao National Laboratory for Marine Science and Technology, Qingdao 266071, China

^c Department of Geosciences, University of Oslo, P.O. Box 1047, Blindern, 0316 Oslo, Norway

^d Research Institute of Petroleum Exploration & Development, Beijing 100083, China

^e The University Centre in Svalbard (UNIS), Pb. 156, 9171 Longyearbyen, Norway

ARTICLE INFO

Article history:

Received 10 December 2015

Received in revised form 20 June 2016

Accepted 5 July 2016

Keywords:

CO₂ induced diagenesis

Dawsonite

Ankerite

Kinetic-thermodynamic modeling

Quantou Formation

Songliao Basin

ABSTRACT

Evidences of CO₂ induced diagenesis in the Quantou Formation, Southern Songliao Basin, have been investigated using petrographic analyses, X-ray diffraction, stable isotopes, fluid inclusions and kinetic-thermodynamic modeling. The studied sandstones have two distinct zones based on their mineralogy, one “pristine” being composed of quartz, plagioclase, chlorite, calcite and dolomite, and one “altered” mainly consisting of quartz, illite and illite/smectite, ankerite, and dawsonite. The ankerite/dawsonite and secondary clay-bearing zones are related to the major deep rooted faults in this area. The δ¹³C value of carbonate cements in the altered zone (mainly centered on -0.9% to -8.0%) is higher than that in the “pristine” sediments. We therefore proposed that these zones have experienced CO₂ charged hydrothermal (~120–140 °C) alteration and with a similar precursor mineral assemblage as in the plagioclase/chlorite rich zones. Kinetic modeling furthermore suggests that the observed alteration must have been under high CO₂ partial pressures, with the closest match between simulations and XRD data found at the highest attempted pressure of 100 bar. The modeling furthermore suggests that using kinetic data from the literature together with reactive surface areas normalized to the surface area of the pores provides good estimates for the alteration of tight sandstones such as the Quantou Fm (~8% porosity).

© 2016 Elsevier Ltd. All rights reserved.

1. Introduction

Mineral carbonatization (MC) is the formation of solid carbonate minerals from aqueous CO₂ or directly from a CO₂ fluid phase. In underground CO₂ storage settings, MC immobilizes CO₂ and thereby reduces the risk for leakages into shallow groundwater aquifers containing potable water, or into the ocean-atmosphere system (Rochelle et al., 2004; Benson and Cole, 2008; Mathias et al., 2013). Mineral reactions are normally regarded slow compared to the timeframes of CO₂ injection, but some studies indicate that some of the mineral reactions may be important on timescales even down to tens of years (Hellevang and Aagaard, 2013). The uncertainties of mineral kinetics models and data, and thereby the

geochemical modeling results, are however large (e.g., Hellevang and Aagaard, 2013), and observations from natural analogues are required to tune kinetic parameters and models.

The Songliao Basin in Northeastern China has a great potential to provide such data on natural CO₂-induced diagenetic reactions. Here, magmatically derived CO₂ or CO₂-charged solutions have migrated through siliciclastic sediments, and earlier works have shown large-scale transformations of the primary minerals into carbonate minerals such as ankerite (Ca(Fe,Mg)(CO₃)₂) and dawsonite (NaAl(OH)₂CO₃) (Gao et al., 2007, 2009; N. Liu et al., 2011; Lu et al., 2011; L. Liu et al., 2011). Similarly in other studies, carbon dioxide of magmatic origin has been mentioned as the possible source of dawsonite formation as a diagenetic mineral in sandstones (Worden, 2006; Golab et al., 2006). Such types of data have been of great importance to understand the conditions required for CO₂ mineral carbonatization and the long-term effects of CO₂ storage, especially the increased understanding of the stability and formation of dawsonite, a mineral that has been predicted to be a major contributor to immobilize CO₂ and provide safe long-term storage (Gao et al., 2007; Hellevang et al., 2014).

* Corresponding authors at: School of Geosciences, China University of Petroleum, Qingdao, Shandong 266580, China.

** Corresponding author at: Department of Geosciences, University of Oslo, P.O. Box 1047, Blindern, 0316 Oslo, Norway.

E-mail addresses: kelai06016202@163.com, xi.kelai@geo.uio.no (K. Xi), cyc8391680@163.com (Y. Cao), helge.hellevang@geo.uio.no (H. Hellevang).

A great deal of information on MC can be learned from studies of 'normal', i.e. temperature and pressure induced diagenesis. First, mineral reactions follow a sequence strictly controlled by temperature, but influenced by the sediment characteristics (grain size, sorting) and composition. The growth of quartz is slow at temperatures below 60–70 °C, and reactions generating silica are therefore inhibited at low temperatures (e.g., transformation of smectite to chlorite) (Bjørlykke and Egeberg, 1993). Ankerite and dawsonite typically occur in sediments that have experienced temperatures of 80 °C or higher (Gao et al., 2009; L. Liu et al., 2011; N. Liu et al., 2011; Hellevang et al., 2014; Pearce et al., 2015a), whereas the kaolinite to illite reaction is prevented at temperatures below approx. 130 °C, probably because of an energy barrier preventing nucleation of the illite fibers (Wilkinson and Haszeldine, 2002). Second, diagenetic reactions are coupled, e.g. transformations of smectite to illite require a potassium source and a silica sink, and the reaction is therefore normally coupled to albitionization of K-feldspar and precipitation of quartz (Lynch et al., 1997; Peltonen et al., 2009; Metwally and Chesnokov, 2012). Quartz growth has been found to be the rate limiting step in these coupled reactions. Finally, mass-balance calculations suggest that most of the diagenetic reactions that take place at burial depths exceeding the influence of meteoric water occur in closed systems with local sources of silica for quartz growth (Bjørlykke and Jahren, 2012). Mineral carbonatization in the Songliao basin may be different in this last aspect of 'normal' diagenesis, as open-system diagenesis and magmatically derived fluids have been required to explain the data (Gao et al., 2009; L. Liu et al., 2011; N. Liu et al., 2011). Even though the open system diagenesis is under continuous dispute, there are studies showing evidences of the possibility of open system diagenesis also of deeply buried sandstones (Barclay and Worden, 2000; Worden and Barclay, 2000; Worden et al., 2015). Furthermore, the Songliao basin may also differ from the normal system as it has been perturbed by magmatic CO₂ that created environments where solid carbonates were added to the system while most silicates got unstable and dissolved (Farquhar et al., 2015; Pearce et al., 2015b).

A recent examination of cores from the Cretaceous Quantou Formation (K₁q) indicates sharp diagenetic boundaries affecting both the silicate and carbonate minerals. Across these boundaries and with increasing burial depth, all chlorite is apparently replaced by smectite (I/S), the inverse of what would be expected in a normal diagenetic system. At the same transition, calcite and dolomite are replaced by a dawsonite/ankerite assemblage. The explanation for this may be CO₂-induced diagenesis, as observed in other parts of the Songliao basin (N. Liu et al., 2011), but there may be other explanations. The carbonates could, for example, be locally sourced and simply formed from the carbonate cements (dolomite or calcite). Another possibility is that these are lithological boundaries rather than diagenetic. The main objective of this study is to increase our understanding of these mineral transitions, using a mass-balance approach, and support the observations with kinetic simulations, and we aim at providing new insight on links between the silicate and carbonate systems with direct relevance to long-term CO₂ storage. Finally, the uncertainties in kinetic simulations are large, and comparing simulated mineral alterations with observations from the Quantou Formation may be used to reduce the uncertainties and build confidence in kinetic simulations of CO₂ storage.

2. Geological background

The Songliao Basin is a Jurassic – Neogene lacustrine basin in the north-eastern China (Fig. 1). The basin is located between 42°25' to 49°23'N and 119°40' to 128°24'E with an area of about 26 × 10⁴ km² (Zhang and Zhang, 2013). It can be further subdivided into seven first class tectonic zones (Zhou et al., 2012), namely the West-

ern Slope Zone, Northern Pitching Zone, Central Depression Zone, Northeastern Uplift Zone, Southeastern Uplift Zone, Southwestern Uplift Zone and Kailu Depression Zone (Fig. 1). The study area, as one of the most oil rich areas, belongs to the Central Depression Zone and consists of three secondary class tectonic units (Li et al., 2013), namely the Changling Sag, Huazijing Terrace and Fuxin Uplift (Fig. 1).

Based on the sediment infilling sequences and structures, the basin evolution can be divided into four phases: (1) a pre-rift phase; (2) a syn-rift phase; (3) a post-rift phase; and finally (4) a compression phase (Zhang et al., 2009). Sediments that have filled the basin comprise the Lower Cretaceous Huoshiling (K₁h), Shahezi (K₁sh), Yingcheng (K₁yc), Doulouku (K₁d) and Quantou (K₁q) formations, the Upper Cretaceous Qingshankou (K₂qn), Yaojia (K₂y), Nenjiang (K₂n), Sifangtai (K₂s) and Mingshui (K₂m) formations, the Palaeogene Yian (Ny) formation, the Neogene Daan (Nd) and Kangtai (Nt) formations, and the Quaternary Pingyuan (Q) formation. Each formation can be further subdivided into different members (Fig. 2). The studied location, that is the fourth member of Quantou formation (K₁q₄), consists mainly of delta sandstones and some interbedded mudstones. According to oil and source rock correlation, the first member of the Qingshankou formation (K₂qn₁), which just overlay the K₁q₄, is the main source rock of the K₁q₄ reservoirs (Li et al., 2013; Zou et al., 2005). In general, K₁q₄ reservoirs are very tight with porosities ranging from 2 to 14% (average 8.5%) and permeabilities ranging from 0.01 to 5 mD (average 0.5 mD).

Previous studies indicated that the Songliao basin was characterized by a high geothermal gradient. From about 90.7 Ma to 65 Ma, the geothermal gradient was 45–55 °C/km and decreases to about 40 °C/km after 65 Ma (Liu, 2004). Data from exploration and production wells furthermore suggest that the maximum burial depth of the Quantou formation was reached 65 Ma ago, and that the maximum temperature reached was about 130 °C (Xi et al., 2015).

3. Databases and methods

3.1. Rock sample analyses

The study was focused on the fourth member of Quantou Formation (K₁q₄) in the southern Songliao basin where most of the producing oil fields occur and consequently most drilling have taken place and core materials, thin sections and many other exploration and production wells data are available. Rock composition data of 743 thin section samples for all the related wells were collected from the Research Institute of Petroleum Exploration & Development of Jilin Oilfield Company, PetroChina.

According to the study objectives and constraints of the collected data, both sandstone and interbedded mudstone samples were selected from the K₁q₄ drill cores from 26 wells. More than 300 polished thin sections and about 210 blue or red epoxy resin-impregnated thin sections were prepared for analyses of rock mineralogy, diagenesis and visual pore characteristics. Thin sections were partly stained with Alizarin Red S and K-ferricyanide for carbonate mineral identification. Point counting was performed on 30 thin sections with at least 300 points to check the correctness of the collected rock composition data, which provided a standard deviation of 5% or less. 88 reservoir sandstone samples and 37 interbedded mudstone samples were analyzed for whole-rock (bulk) and clay fraction (<2 µm) mineralogy using XRD. Preparation, analyses and interpretation procedures were modified from Moore and Reynolds (1997) and Hillier (2003). About 5.0 g of each sample were crushed, milled in ethanol in a McCrone micronizing mill and then dried at 60 °C. Randomly oriented powders were prepared by top-loading into PMMA (Polymethylmethacry-

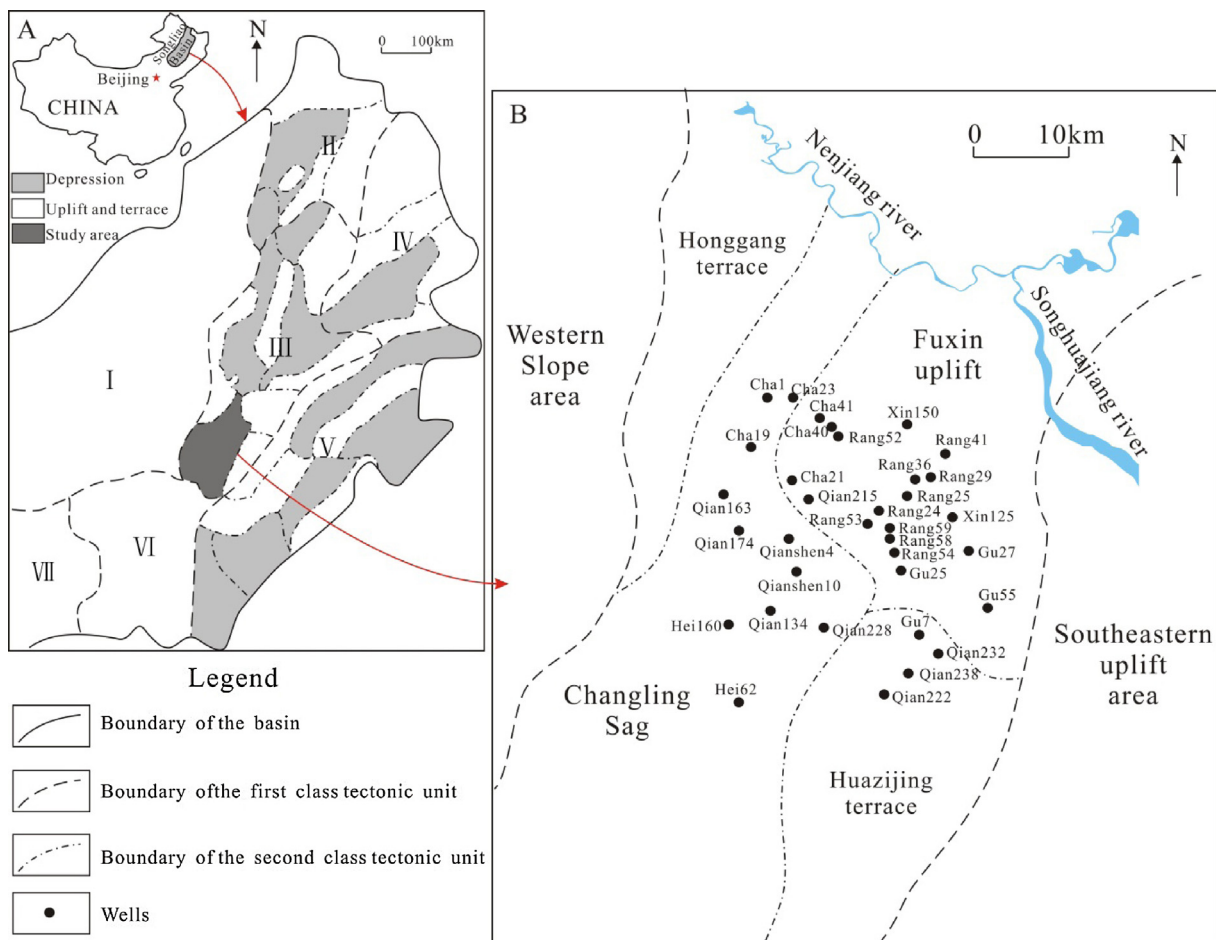


Fig. 1. (A) Location map of the study area and sub-tectonic units of the Songliao Basin (I) Western Slope Zone, (II) Northern Pitching Zone, (III) Central Depression Zone, (IV) Northeastern Uplift Zone, (V) Southeastern Uplift Zone, (VI) Southwestern Uplift Zone, (VII) Kailu Depression Zone; (B) The sub-tectonic units of the study area and well locations.

From [Xi et al. \(2015\)](#).

late) sample holders designed with concentric circular geometry grooved shallow wells. The powder diffraction patterns were collected using a D/MAX 2500 X-ray diffractometer with Cu K α radiation. All XRD data were first analyzed for phase identification with the search-match module of the EVA software using the reference data bases ICDD PDF-2 and COD. After phases were identified, they were further analyzed based on the Rietveld quantitative X-ray diffraction refinement approach. 31 representative samples were viewed under a Quanta FEG 450 and SU 5000 scanning electron microscope (SEM) equipped with an energy dispersive X-ray spectrometer (EDS). The quantitative data provided are given as XRD%, hereafter simplified to '%' in the remaining text.

A total of 37 core samples from 12 wells were prepared as thick doubly polished thin sections for fluid inclusion petrographic analyses and microthermometric measurements. The fluid inclusions provide valuable information for continuous fluid activities in the sandstones during burial process ([Robinson and Gluyas, 1992](#)). Microthermometry of fluid inclusions was conducted using a petrographic microscope equipped with a Linkam THMSG 600 heating and cooling stage which enables temperatures of phase transitions in the range of -180 to 500 °C. Homogenization temperatures (Th) were determined using a heating rate of 10 °C/min when the temperature was lower than 50 °C and a rate of 5 °C/min when the temperature exceeded 50 °C. Precision was ± 1 °C for homogenization temperatures. Based on the petrological studies,

87 organic-matter-free sandstone samples and 30 interbedded mudstone samples were chosen for carbon and oxygen stable isotope analyses. Samples were disaggregated directly with a hammer and then crushed in a mortar. Then the disaggregated samples were sieved to pass through a 200 mesh sieve (75 μm) to get the powder. Finally, these powdered samples were analyzed using a ThermoFinnigan MAT 253 isotope ratio mass spectrometer. Precision was $\pm 0.08\%$ for $\delta^{18}\text{O}$ and $\pm 0.06\%$ for $\delta^{13}\text{C}$. Carbon and oxygen stable isotope data are presented in the δ notation relative to the Vienna PeeDee Belemnite (V-PDB) standards. For Jurassic and younger samples, the best discrimination between marine and fresh-water carbonate is given by the equation by [Keith and Weber \(1964\)](#):

$$Z = a(\delta^{13}\text{C} + 50) + b(\delta^{18}\text{O} + 50) \quad (1)$$

In which a and b are 2.048 and 0.498 respectively. Point counting, thin section observation and fluid inclusion analyses were done in the Basin Analysis and Reservoir Geology Key Laboratory of China University of Petroleum. XRD and SEM were done in the Key Laboratory of Oil and Gas Reservoir of PetroChina and University of Oslo. Carbon and oxygen stable isotope testing was done in the Analytical Laboratory of CNNC Beijing Research Institute of Uranium Geology.

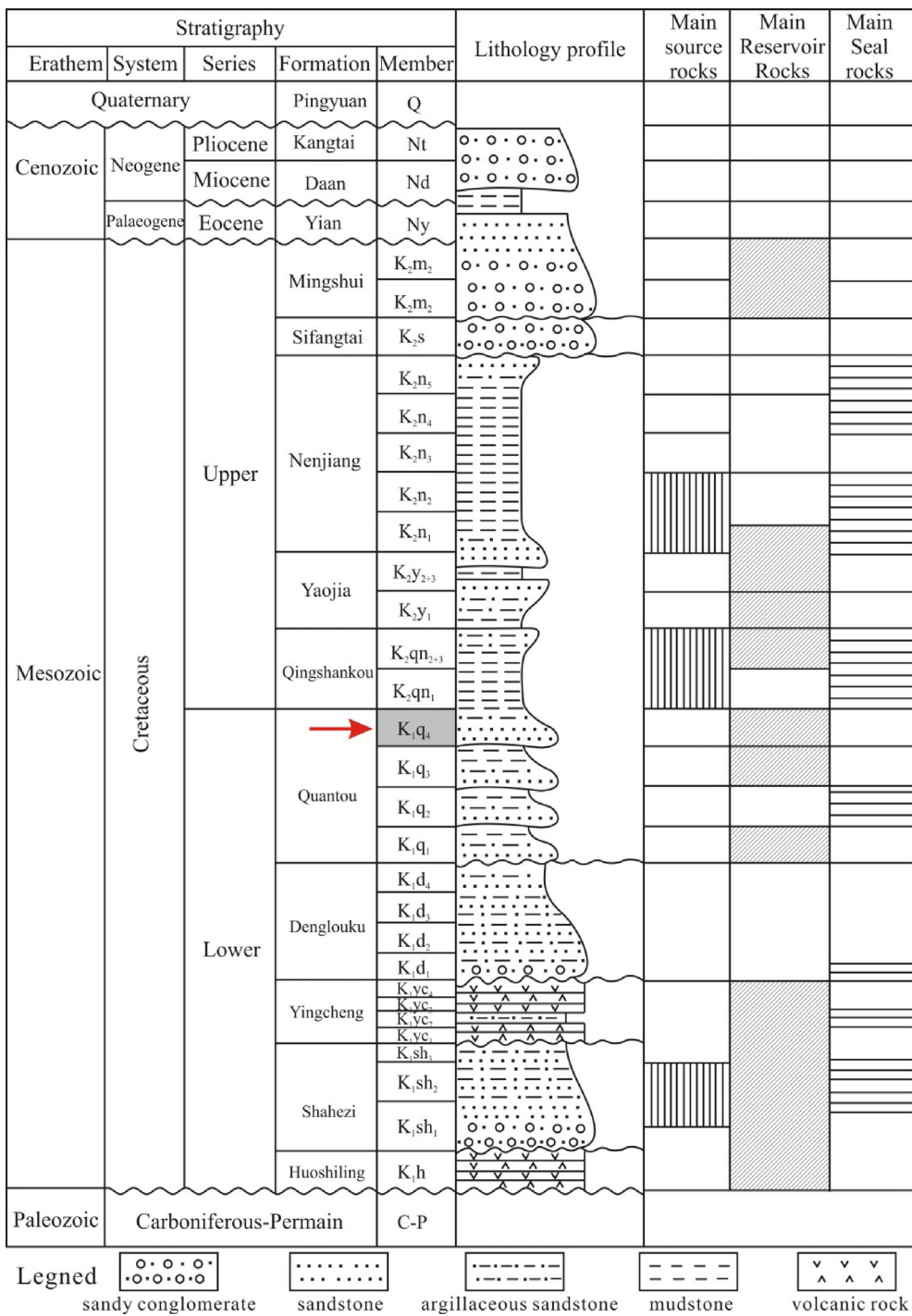


Fig. 2. Generalized Mesozoic-Quaternary stratigraphy of the Songliao Basin, showing major oil and gas combinations.

From [Xi et al. \(2015\)](#).

3.2. Kinetic modeling

To understand the apparent transformation of chlorite and feldspar into ankerite and dawsonite, we performed kinetic simulations using the PHREEQC 3.0 software and applying the [phreeqc.dat](#) database ([Parkhurst and Appelo, 2013](#)). Thermodynamic data for phases that are not listed in [phreeqc.dat](#) have been copied from literature (e.g. ankerite from [Gysi and Stefánsson, 2011](#), and dawsonite from the [Ilnl.dat](#) phreeqc database) and is supplied in the example input file (Supplementary). An example input file is pro-

vided as Supplementary material to the paper. There are indications that the temperature of the Quantou Fm. has been at around 100 °C or even higher ([Xi et al., 2015](#)) and we therefore used a Transition-State-Theory (TST) based rate model ([Aagaard and Helgeson, 1982](#)) for the dissolution of chlorite and feldspar:

$$r_+ = k_+ S a_{H^+}^\nu (1 - \Omega), \quad (2)$$

where k_+ (mol/m²s) is the rate constant at pH 0, S is the reactive surface area (m²), a_{H^+} denotes aqueous activity of H⁺, and Ω is the saturation ratio ($\Omega = q/K$, where q is the ion activity product and K is

Table 1

Kinetic parameters used for the dissolving plagioclases and chlorite.

Mineral	$\log k^0$ (mol/m ² s)	E_a (kJ/mol)	v^b
Plagioclase (oligoclase)	-9.67	65.0	0.457
Chlorite (clinochlore-14A)	-11.11	88.0	0.5

From [Palandri and Kharaka \(2004\)](#).

^a Rate constant at 25 °C and pH 0.

^b pH dependency of dissolution rates (see Eq. (2)).

the equilibrium constant). Rate constants at elevated temperatures were calculated according to:

$$k_+ = k^0 \exp \left\{ -\frac{E_a}{R} \left(\frac{1}{T} - \frac{1}{T^0} \right) \right\}, \quad (3)$$

where E_a is the apparent activation energy (J/mol), R is the gas constant (8.3145 J/mol K), and T is absolute temperature. Superscript 0 denotes the reference temperature 298.15 K. Rate parameters for the dissolving phases were taken from [Palandri and Kharaka \(2004\)](#) and are listed in [Table 1](#). Secondary phases were assumed to form fast and according to the local-equilibrium assumption ([Helgeson, 1967](#)). The reactive assemblage and possible secondary phases was based on a simple inverse estimate of difference in masses (mol/L pore space) between the dawsonite/ankerite bearing parts of the sandstone (hereafter referred to as the altered parts), and the parts having chlorite and abundant plagioclase (hereafter referred to as the pristine parts). With the exception of the carbonate system, we assumed that the altered parts had the same origin as the pristine sediments, but that fault-related fluids were constrained only to the altered parts. As will be shown it was indicated, both from the mass-balance calculations and petrographic observations, that dolomite rather than calcite was the main source for ankerite. Perhaps, Fe-rich calcite had replaced primary dolomite in the pristine zones. We therefore used dolomite as a reactive kinetic phase rather than calcite. The inverse estimates are provided as part of the results below. The timeframe of the observed alteration is not known, but we assumed that the system must have been active for at least thousands of years as the magmatic system was active for ~40,000–50,000 years ([Lu et al., 2011](#)), and we used 50,000 years for the simulations. Reactive surface areas for the plagioclase and chlorite were estimated based on the method suggested for tight rocks in [Hellevang and Aagaard \(2013\)](#):

$$S_{+,i} = \frac{3000\xi_i x_i \alpha}{r_\phi}, \quad (4)$$

where ξ is the pore surface roughness factor, x is the volume fraction of mineral i , α is the fraction of the total surface area that is reactive, and r_ϕ is the average pore size radius (μm). The average pore radius for the rocks was estimated to 144 μm (according to rate-controlled mercury injection), and we made a first rough estimate of the surface areas using surface roughness factors of 0.1 and 10 for plagioclase and chlorite respectively, and α values of 1.0, and this resulted in reactive surface areas of 0.512 and 10.83 m²/kgw for the plagioclase and chlorite respectively. These surface areas were then modified (reduced) by changing α until the simulated alteration matched well with the observed dissolved amount of plagioclase (Δmol/L water). For the simulations, the temperatures range of 100–140 °C was used and the CO₂ fugacity was varied from 1.0 to 100 bar. CO₂ fugacities were calculated using the SRK-EoS ([Soave, 1972](#)) included in the latest version of phreeqc. The algorithm also includes accurate estimates of the effect of pressure on the equilibrium constants, providing the required Poynting correction to the CO₂ solubility (see [Hellevang and Kvamme, 2006](#) and comparisons to solubility data by [Duan and Sun, 2003](#)). Because the simulated system is in a lacustrine setting, we approximated the hydrothermal fluid using a freshwater solution equilibrated

Table 2

Initial formation water based on diluting seawater to 25% of the original salinity, reducing the oxygen, and adding an initial HCO₃⁻ corresponding to measurements in the “pristine” sediments. The NaCl and HCO₃⁻ were based on a formation water sample from well Cha19 at 2282 m depth. The sample was incomplete and we therefore based our diluted seawater composition on [Nordstrom et al. \(1979\)](#).

	ppm
Al	0.0
HCO ₃ ⁻	1200
Ca	103.1
Fe	0.0005
K	100
Mg	323
Na	2692 ^a
Si	1.07
pH	7.0
log PCO ₂	-0.38

^a Charge balanced to achieve pH 7.

with the CO₂ pressures and the primary minerals quartz, kaolinite, K-feldspar, and dolomite. The solution was not equilibrated with chlorite and plagioclase as they were defined as kinetic reactants. The solution composition in equilibrium with CO₂ and the primary minerals is given in [Table 2](#).

4. Results and discussion

The sandstones are fine to medium-grained ([Fig. 3A](#)). Sorting ranges from moderate to well sorted, and roundness of the detrital grains varies from sub-angular to sub-rounded ([Fig. 3A](#)). According to point counting, the sandstones are mostly lithic arkoses and feldspathic litharenites, compositionally immature with an average framework composition of Q₄₃F₂₆R₃₁ ([Fig. 3B](#)). The sediments were divided into two domains because of distinct characteristics within each of these domains. The transition from one domain to the other is sharp, with abrupt changes in the carbonate, feldspar and clay mineralogy ([Figs. 4 and 5](#)), and we suggest that this may be caused by differences in the diagenesis rather than being of depositional origin. This is further discussed below. The mineral alteration patterns share some similarities to those observed earlier for CO₂-induced diagenesis in the Songliao Basin (e.g., [Gao et al., 2009](#); [Liu et al., 2011](#); [N. Liu et al., 2011](#)), and we have therefore divided the results below into “pristine” and “CO₂-altered” sediments. The CO₂-alteration hypothesis is investigated below running PHREEQC alteration simulations.

4.1. Characterization of “pristine” sediments apparently not altered by CO₂

In the sandstone reservoirs, the majority of the detrital quartz grains are monocrystalline. The quartz content varies between 17.8 and 65.1% with a mean value of 48.6%, showing no significant trend with depth. K-feldspar and plagioclase (mainly albite) are two kinds of major feldspar in the study area. The average of K-feldspar content is 5.8%, varying from 0.7 to 16.9%. The content of the plagioclase ranges from 13.9 to 37.7%, with an average of 24.62%. Calcite, the major carbonate in the “pristine” sediments, varies from 0 to 40.1%,

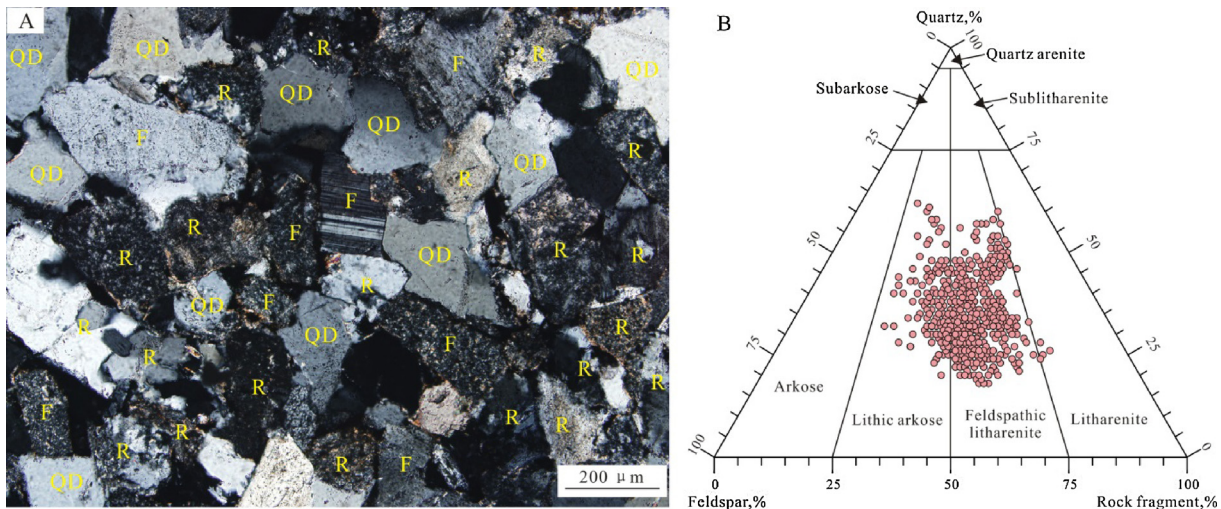


Fig. 3. Rock composition of the K₁q₄ tight sandstone reservoirs: (A) Micrograph of thin section showing quartz, feldspar and volcanic rock fragments; (B) Classification of sandstone using Folk's (1974) classification. QD—detrital quartz; F—feldspar; R—volcanic rock fragment.

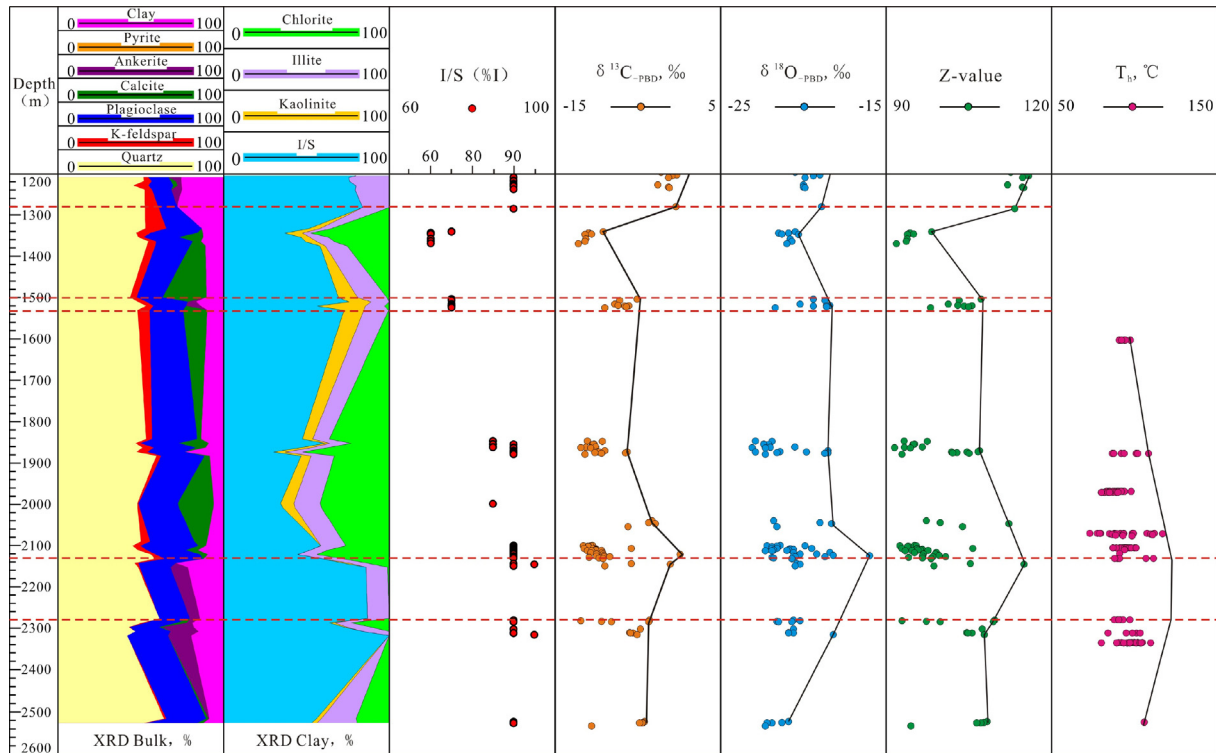


Fig. 4. Mineralogical composition (bulk and clay fraction), carbon and oxygen isotope, Z-value and homogenization temperature distribution characteristics as a function of depth in the reservoir sandstones. T_h—homogenization temperature; I/S—mixed-layer illite/smectite; I—illite.

with an average of 5.9%. Most of the “pristine” sediment does not contain any ankerite (Fig. 4; Table 3). Dolomite was observed in well Hei 62 where it was quite abundant (about 9–14%). Kaolinite, mixed-layer I/S, illite and chlorite are the common clay minerals. The total clay content ranges from 4.1 to 57.4% with an average of 15.1%. Kaolinite is a minor phase and mainly occurs as euhedral booklets and vermicular aggregates, whose content varies from 0 to 1.8% with an average of 0.44%. Mixed-layer I/S interstratified with R=1 and R=3 (R denotes Reichweite order) is the dominating clay mineral and mainly occurs as foliated or honeycomb aggregates, whose content ranges from 1.9 to 40.8% with an average of 7.6%.

Illite occurs as honeycomb, flaky crystal and sometimes as acicular crystals, and varies between 0.3 and 9.2% with a mean value of 1.8%. Chlorite is also an important clay mineral in the “pristine” sediments. The average of chlorite content is 5.2%, varying from 1.0 to 13.1% (Fig. 4; Table 4).

The interbedded mudstones in the “pristine” sediments contain the same mineral types but in different relative quantities (Fig. 5), in which quartz ranges from 12.7 to 39.8% with an average of 26.2%, K-feldspar ranges from 0.2 to 5.1% with an average of 1.1%, plagioclase ranges from 7.5 to 21.9% with an average of 13.0%, calcite ranges from 0 to 7.4% with an average of 1.8%. Ankerite, pyrite and siderite

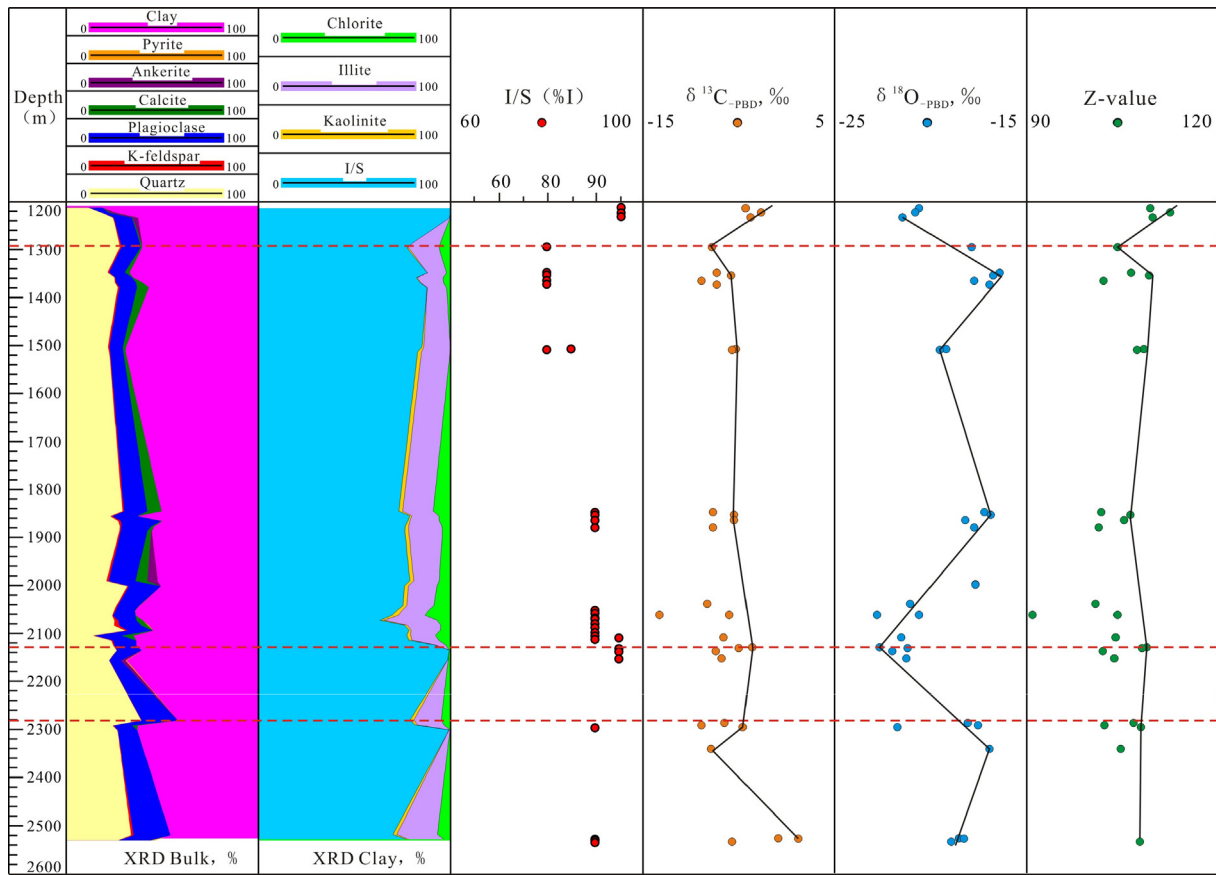


Fig. 5. Mineralogical composition (bulk and clay fraction), carbon and oxygen isotope and Z-value distribution characteristics as a function of depth in the interbedded mudstones.
I/S—mixed-layer illite/smectite; I—illite.

are only present in trace amounts. The total clay content ranges from 40.3 to 67.4% with an average of 56.6%. The clay is dominated by mixed-layer I/S constituting 43.5 XRD%, varying from 30.36 to 55.09%. The remaining clay is composed of kaolinite (0.85%, varying from 0 to 3.6%), illite (8.8%, varying from 5.2 to 16.9%), Chlorite (3.4%, varying from 1.0 to 15.2%) (Fig. 5).

The porosity of the samples from the wells without CO_2 varies between 3.0 and 13.0% with an average of 8.4%, and the permeability of these samples ranges from 0.01 mD to 0.65 mD, with a mean value of 0.15 mD (Fig. 6).

4.2. Characterization of CO_2 -altered zones

The CO_2 -altered zones are mainly distributed in the intervals around 1280m, between about 1500 and 1530m and between about 2130 and 2280m. In the sandstone reservoirs, the morphology characteristics of the minerals are similar to the “pristine” sediments. The quartz content varies between 28.3 and 64.4% with a mean value of 49.9%, showing no significant trend with depth. The average of K-feldspar content is 3.1%, varying from 0 to 12.2%. The content of the plagioclase ranges from 3.6 to 34%, with an average of 18.2%. Calcite content ranges from 0 to 27.1% with a mean value of 1.64%. Ankerite, the major carbonate in the CO_2 altered zones, varies from 0 to 28.5%, with an average of 6.0% (Fig. 4; Table 5). Partly dissolved dolomite is found in association with the secondary ankerite and may be a precursor for the ankerite growth (Fig. 7). It was difficult to separate the ankerite from dolomite, and all quantities in Table 5 were therefore listed as ankerite. The total clay content ranges from 9.5 to 52.4% with an average of 20.7%. Kaolinite content varies from 0 to 4.5% with an average of 0.9%. Mixed-layer

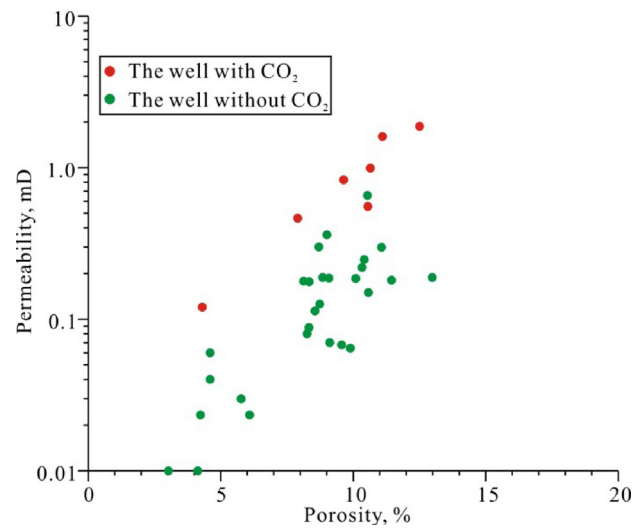


Fig. 6. The comparison of reservoir porosity and permeability between the wells with CO_2 and without CO_2 .

I/S, interstratified with R = 3, ranges from 4.9 to 52.4% with an average of 16.7%. Illite content varies between 0 and 8.1% with a mean value of 2.8%. However, the content of chlorite is much lower than that in the “pristine” sediments. Only a few samples contain chlorite, whose content varies from 0 to 4.5%, with a mean value of 0.3% (Fig. 4; Table 6).

Table 3

Bulk XRD of sandstones in the “pristine” sediments.

Well	Depth, m	Quartz, %	K-feldspar, %	Plagioclase, %	Calcite, %	Ankerite, %	Pyrite, %	Siderite, %	Clay, %
Cha10	1998.57	47.8	0.7	23.6	22	0	0	0	5.9
Cha19	2282.45	38.5	0.9	16.9	28.7	0	0	0	15
Cha19	2284.35	61.2	5.9	13.9	4.5	3.5	0	0	11
Cha19	2285.15	52.3	2.2	19.4	7.2	0	0	0	18.9
Hei160	2523.08	53.9	7	22.2	7.3	0	0	0	9.6
Hei160	2525.25	65.1	1.4	24	1.5	0	0	0	8
Hei160	2526.1	50.8	1.3	31.5	3.7	0	0	0	12.7
Hei160	2526.4	50.2	2.4	29.9	6	0	0	0	11.5
Hei160	2533.9	53.8	2.7	18.1	14.1	0	0	0	11.3
Rang24	1846.09	53.3	3.6	27.3	2.1	0	0	0	13.7
Rang24	1847.3	41.9	12.1	19.4	17.3	0	0	0	9.3
Rang24	1853.7	44.3	2.8	21.7	23.9	0	0	0	7.3
Rang24	1854	64.1	4.5	25.3	0.5	0	0	0	5.6
Rang24	1854.35	50.2	7.9	28.2	4.4	0	0	0	9.3
Rang24	1860.8	51.6	6.6	29.9	0	0	0	0	11.9
Rang24	1861.3	50.7	13.3	25.3	2	0	0	0	8.7
Rang24	1862.7	50.6	6.9	23	8.9	0	0	0	10.6
Rang24	1863.5	47.9	2.7	23	21.9	0	0	0	4.5
Rang24	1869.3	46.1	4.4	22.6	1.8	0	0	0	25.1
Rang24	1872.2	59.4	5.6	24.7	0.7	0	0	0	9.6
Rang24	1872.4	46.8	6.5	22.4	0	0	0	0	24.3
Rang24	1872.7	56.3	7.1	25.2	0	0	0	0	11.4
Rang24	1874.02	52.9	6.7	24.1	1.7	0	0	0	14.6
Rang24	1875.12	37.1	5.1	33.5	0.5	0	0	0	23.8
Rang24	1875.63	63	2.8	20.1	0	0	0	0	14.1
Rang24	1878.35	59.8	3	26.2	2.5	0	0	0	8.5
Rang59	2099.77	50.3	6.1	27	6.2	0	0	0	10.4
Rang59	2100.54	33.7	5	26.3	18.7	0	0	0	16.3
Rang59	2100.94	43.4	4.3	37.6	3.9	0	0	0	10.8
Rang59	2101.76	53.3	3.8	27.3	3.1	0	0	0	12.5
Rang59	2102.98	52.3	5.2	26.9	3.1	0	0	0	12.5
Rang59	2106.75	27.2	5.2	22.5	10.1	0	0	0	35
Rang59	2107.2	51.4	13.1	23.9	0.3	0	0	0	11.3
Rang59	2108.11	52.3	9.3	23.4	0.6	0	0	0	14.4
Rang59	2109.14	27.8	5.4	24.4	3.4	0	0	0	39
Rang59	2109.91	44.7	9	30.1	4.6	0	0	0	11.6
Rang59	2111.04	48.2	5.3	23.7	7.2	0	0	0	15.6
Rang59	2111.79	60.8	6.4	20.1	0.4	0	0	0	12.3
Rang59	2112.42	52.9	3.5	20.5	9.5	0	0	0	13.6
Rang59	2112.6	48.7	10.3	17.7	16.2	0	0	0	7.1
Rang59	2116.34	38.5	16.9	24.5	0.1	0	0	0	20
Rang59	2116.84	42.8	6.1	28.6	0	0	0	0	22.5
Rang59	2117.81	46.4	11.6	24.4	0	0	0	0	17.6
Rang59	2120.59	31.9	5.9	37.7	0.1	0	0	0	24.4
Rang59	2121.1	56.7	2.8	26.9	4.9	0	0	0	8.7
Rang59	2125.72	48.3	3	25.8	2.6	0	0	0	20.3
Rang59	2127.25	37.1	11.2	29.2	0	0	0	0	22.5
Rang59	2128.5	60.6	5.4	21.6	2.3	0	0	0	10.1
Rang59	2129.91	27.5	4.4	20.9	10.3	0	0	0	36.9
Rang59	2130.17	17.8	1.9	20.6	2.3	0	0	0	57.4
Xin125	1340	60	2.3	25.2	0.4	0	0	0	12.1
Xin125	1341	52.8	13.3	23	0	0	0	0	10.9
Xin125	1343	52.6	7.1	26.7	4.4	0	0	0	9.2
Xin125	1343.6	41.7	10.4	29.8	1.8	0	0	0	16.3
Xin125	1345.32	54.5	8.2	22.3	0.6	0	0	0	14.4
Xin125	1346.4	34.9	2.9	18	40.1	0	0	0	4.1
Xin125	1357.5	55.4	3.9	23.2	0.7	0	0	0	16.8
Xin125	1363.57	54.3	1	30.3	0.5	0	0	0	13.9
Xin125	1369	54.1	5.1	21.3	8.4	0	0	0	11.1
Average		48.55	5.79	24.62	5.93	0.05	0	0	15.05

In the interbedded mudstones of the CO₂ altered zones the content of quartz ranges from 11.6 to 19.0% with an average of 22.6%, K-feldspar ranges from 0.1 to 0.8% with an average of 0.4%, plagioclase ranges from 2.2 to 13.6% with an average of 8.4%, calcite ranges from 0 to 1.5% with an average of 0.4%, ankerite varies from 0 to 2.9% with an average of 0.8%. The total clay content ranges from 56.1 to 81.3% with an average of 64.0%. As for the pristine sediments, the CO₂-altered mudstones are dominated by mixed-layer I/S constituting 56%, varying from 0 to 81.3%. The remaining clay contained kaolinite (0.19%, varying from 0 to 1.3%), illite (7.7%, varying from 0 to 58.7%), chlorite (0.1%, varying from 0 to 0.7%) (Fig. 5).

The porosity of the samples from the wells with CO₂ varies between 4.3 and 12.5% with an average of 9.52%, and the permeability of these samples ranges from 0.12 mD to 1.87 mD, with a mean value of 0.92 mD (Fig. 6).

4.3. Diagenetic mineralogy

Authigenic minerals in the K₁q₄ sandstones mainly contain quartz, ferrocalcite, ankerite, dawsonite and clay minerals (Fig. 7). There are some obvious differences in the authigenic minerals between the “pristine” sediments and the CO₂ altered zones.

Table 4

Clay mineral XRD of sandstones in the “pristine” sediments.

Well	Depth, m	I/S, %	I, %	K, %	C, %	I/S (%)
Cha10	1998.57	2.01	0.94	0.47	2.48	15
Cha19	2282.45	9.45	1.20	0.60	3.75	25
Cha19	2284.35	6.93	0.88	0.55	2.64	30
Cha19	2285.15	10.96	1.70	0.76	5.48	25
Hei160	2523.08	5.18	2.11	0.29	2.02	10
Hei160	2525.25	4.08	2.40	0.32	1.20	10
Hei160	2526.1	7.49	3.18	0.51	1.52	10
Hei160	2526.4	6.67	2.99	0.46	1.38	10
Hei160	2533.9	6.78	1.70	0.45	2.37	15
Rang24	1846.09	6.44	1.37	0.82	5.07	15
Rang24	1847.3	5.39	1.12	0.28	2.51	15
Rang24	1853.7	5.04	1.10	0.15	1.02	15
Rang24	1854	1.90	0.45	0.50	2.74	10
Rang24	1854.35	5.30	1.30	0.37	2.33	15
Rang24	1860.8	5.24	1.07	0.83	4.76	15
Rang24	1861.3	4.09	0.70	0.61	3.31	15
Rang24	1862.7	4.03	0.53	0.95	5.09	10
Rang24	1863.5	1.98	0.32	0.18	2.03	10
Rang24	1869.3	7.28	3.01	1.76	13.05	10
Rang24	1872.2	3.26	0.58	0.67	5.09	10
Rang24	1872.4	8.75	2.43	1.70	11.42	10
Rang24	1872.7	5.13	0.68	0.80	4.79	10
Rang24	1874.02	7.30	0.88	0.88	5.55	10
Rang24	1875.12	10.23	2.38	1.19	10.00	10
Rang24	1875.63	3.38	0.99	1.27	8.46	10
Rang24	1878.35	4.00	1.19	0.51	2.81	10
Rang59	2099.77	6.14	1.56	0.00	2.70	10
Rang59	2100.54	11.57	2.28	0.00	2.45	10
Rang59	2100.94	6.05	1.40	0.00	3.35	10
Rang59	2101.76	6.75	1.50	0.00	4.25	10
Rang59	2102.98	5.88	1.25	0.00	5.38	10
Rang59	2106.75	23.45	5.95	0.00	5.60	10
Rang59	2107.2	2.94	1.13	0.00	7.23	10
Rang59	2108.11	5.04	1.30	0.00	8.06	10
Rang59	2109.14	26.91	4.68	0.00	7.41	10
Rang59	2109.91	4.87	1.62	0.00	5.10	10
Rang59	2111.04	4.99	1.56	0.00	9.05	10
Rang59	2111.79	6.27	0.86	0.00	5.17	10
Rang59	2112.42	5.17	1.36	0.00	7.07	10
Rang59	2112.6	3.12	0.50	0.00	3.48	10
Rang59	2116.34	8.80	2.00	0.00	9.20	10
Rang59	2116.84	10.13	2.25	0.00	10.13	10
Rang59	2117.81	5.81	1.76	0.00	10.03	10
Rang59	2120.59	14.64	3.42	0.00	6.34	10
Rang59	2121.1	3.57	0.70	0.00	4.44	10
Rang59	2125.72	9.74	2.03	0.00	8.53	10
Rang59	2127.25	7.43	2.93	0.00	12.15	10
Rang59	2128.5	4.04	0.81	0.00	5.25	10
Rang59	2129.91	26.20	5.54	0.00	5.17	10
Rang59	2130.17	40.75	9.18	0.00	7.46	10
Xin125	1340	5.45	0.61	0.97	5.08	25
Xin125	1341	3.92	0.55	1.20	5.23	25
Xin125	1343	4.23	0.92	0.74	3.31	30
Xin125	1343.6	8.64	1.14	1.30	5.22	30
Xin125	1345.32	5.76	1.30	1.15	6.19	30
Xin125	1346.4	1.85	0.49	0.21	1.56	30
Xin125	1357.5	8.23	1.68	1.01	5.88	30
Xin125	1363.57	6.95	1.53	0.97	4.45	30
Xin125	1369	6.44	1.44	0.33	2.89	30
Average		7.63	1.77	0.44	5.21	

K—kaolinite; I—illite; I/S—mixed-layer illite/smectite; C—chlorite; S—smectite.

Authigenic quartz occurs in two different types of morphologies and is generally the most abundant cement in both domains. One morphology is partial to complete syntaxial overgrowths, which is easy to discriminate from the detrital grains due to the existence of dust rims (Fig. 7A). The other morphology is pore-filling cement and difficult to distinguish from grains by the polarizing microscope (Fig. 7B). The quartz cement in the tight sandstone reservoirs mainly occurs as relatively large aggregates

of microcrystalline or macrocrystalline euhedral authigenic quartz approximately 30–100 μm in size (Fig. 7A and B).

Ferrocalcite and ankerite are two kinds of volumetric predominant carbonate cements. They occur as scattered euhedral rhombs, pore-filling blocky or mosaic aggregates (Fig. 7C–F). Ankerite mainly exists in the CO₂ altered zones whereas ferrocalcite are mainly present in the “pristine” sediments. Another kind of carbonate cement, dawsonite, can only be seen in the CO₂ altered zones. The dawsonite show acicular habitus forming aggregates

Table 5Bulk XRD of sandstones in the CO₂ altered zones.

Well	Depth, m	Quartz, %	K-feldspar, %	Plagioclase, %	Calcite, %	Ankerite, %	Pyrite, %	Siderite, %	Clay, %
Gu27	1195.64	47.2	1.5	16.5	0	13	0	0	21.8
Gu27	1202.17	60.6	2.1	3.6	0	0	0	0	33.7
Gu27	1204.6	63.4	3.1	9.7	0	0	0	0	23.8
Gu27	1208.42	51.6	2.8	12.4	0	7.7	0	0	25.5
Gu27	1226.4	52.1	6.2	11	4.9	0	0	0	25.8
Gu27	1232.16	38.5	12.2	19.2	0	5.5	0	0	24.6
Gu27	1233.62	52.3	4	11.7	0	7.4	0	0	24.6
Gu27	1279.42	52.5	7.9	11.3	0	0	0	0	28.3
Gu31	1503.45	43.2	3.9	15.5	27.1	0	0	0	10.3
Gu31	1506.4	46.7	5.4	27.9	0	0	0	0	20
Gu31	1515.5	50.8	4.6	19.6	0.3	15.2	0	0	9.5
Gu31	1518.1	64.4	6.5	19.1	0	0	0	0	10
Gu31	1519	53.3	5.9	22.8	0	0	0	0	18
Gu31	1520.2	53.1	3.2	17.6	0	15.7	0	0	10.4
Gu31	1521.99	59.8	3.2	20.8	0	0	0	0	16.2
Gu31	1524.19	48	7.4	20	14.8	0	0	0	9.8
Cha10	2280.75	61.6	0	18.4	0	6.1	0	0	13.9
Cha10	2284.49	46.4	0	14.9	0	12.2	0	0	26.5
Cha10	2302	39.7	0	17.4	0	25.2	0	0	17.7
Cha10	2311.15	50	0	23.2	0	12.7	0	0	14.1
Cha10	2312.26	48.2	0	34	0	0	0	0	17.8
Cha10	2312.37	41.1	0	24.6	0	14.4	0	0	19.9
Cha10	2316.04	28.3	0	15.2	0	0	0	4.1	52.4
Cha21	2107.4	48.8	1.5	22.2	0	0	1.8	0	25.7
Cha21	2127.3	58.1	1	20.3	0	0	0	0	20.6
Cha21	2132.1	58.4	5.8	23.2	0.4	0	0	0	12.2
Cha21	2144	40	0.5	13.8	0	28.5	6.7	0	10.5
Cha21	2145.8	41.8	1.2	22.3	0	0	0	0	34.7
Cha21	2149.25	48.1	1	18.5	0	10.5	0	0	21.9
Average		49.93	3.13	18.16	1.64	6.01	0.29	0.14	20.69

Table 6Clay mineral XRD of sandstones in the CO₂ altered zones.

Well	Depth, m	I/S, %	I, %	K, %	C, %	I/S (S%)
Gu27	1195.64	18.53	3.27	0.00	0.00	10
Gu27	1202.17	25.61	8.09	0.00	0.00	10
Gu27	1204.6	18.33	5.47	0.00	0.00	10
Gu27	1208.42	18.62	6.89	0.00	0.00	10
Gu27	1226.4	20.64	5.16	0.00	0.00	10
Gu27	1232.16	19.68	4.67	0.00	0.25	10
Gu27	1233.62	19.43	5.17	0.00	0.00	10
Gu27	1279.42	23.77	4.53	0.00	0.00	10
Gu31	1503.45	7.21	1.85	1.24	0.00	25
Gu31	1506.4	15.40	2.20	2.40	0.00	25
Gu31	1515.5	5.32	1.05	3.14	0.00	25
Gu31	1518.1	5.70	1.20	2.70	0.40	25
Gu31	1519	12.78	1.44	3.78	0.00	25
Gu31	1520.2	4.89	1.04	4.47	0.00	25
Gu31	1521.99	9.88	1.94	4.37	0.00	25
Gu31	1524.19	7.15	1.47	1.18	0.00	25
Cha10	2280.75	12.09	1.81	0.00	0.00	10
Cha10	2284.49	22.79	3.71	0.00	0.00	10
Cha10	2302	14.51	3.19	0.00	0.00	10
Cha10	2311.15	12.27	1.83	0.00	0.00	10
Cha10	2312.26	16.38	1.25	0.00	0.18	10
Cha10	2312.37	17.11	2.79	0.00	0.00	10
Cha10	2316.04	52.40	0.00	0.00	0.00	5
Cha21	2107.4	18.76	3.86	0.51	2.57	10
Cha21	2127.3	17.72	2.68	0.00	0.21	10
Cha21	2132.1	5.86	0.85	0.98	4.51	30
Cha21	2144	8.93	1.37	0.11	0.11	10
Cha21	2145.8	34.35	0.00	0.00	0.35	5
Cha21	2149.25	18.83	2.85	0.00	0.22	10
average		16.72	2.81	0.86	0.3	

K—kaolinite; I—illite; I/S—mixed-layer illite/smectite; C—chlorite; S—smectite.

and is always accompanied by ankerite. The dawsonite apparently replaces the detrital feldspars (Fig. 7G–L). Point counting analysis reveals that dawsonite is present in volumes of 0.5–4%.

Ankerite is seen to always partially or completely replace dolomite (Fig. 7M–O).

Various types of clay minerals with different amounts and textural habits occur in the K₁q₄ tight sandstone reservoirs as

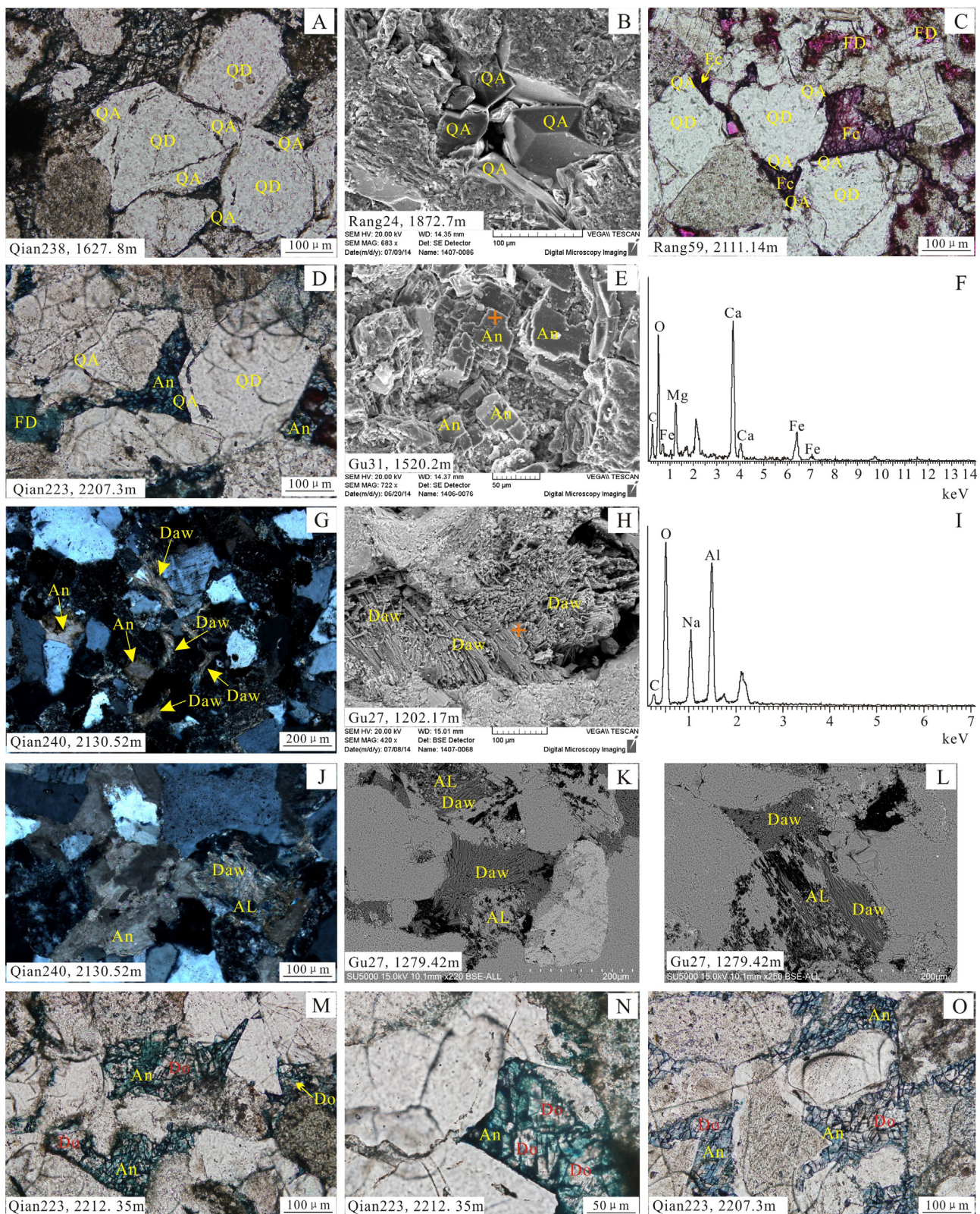


Fig. 7. Diagenetic mineralogy characteristics in K₁q₄ tight sandstone reservoirs. (A) Micrograph of thin section showing the quartz overgrowth; (B) Micrograph of SEM showing the quartz overgrowth; (C) Micrograph of thin section showing the ferrocalcite; (D) Micrograph of thin section showing the ankerite; (E) Micrograph of SEM showing ankerite; (F) The EDS of mark site in E showing the ankerite; (G) Micrograph of thin section showing the dawsonite and ankerite; (H) Micrograph of SEM showing the dawsonite; (I) The EDS of mark site in H showing the dawsonite; (J) Micrograph of thin section showing albite dissolution and dawsonite forming. (K and L) Micrographs of SEM showing albite dissolution and dawsonite forming; (M–O) Micrographs of thin section showing the conversion of dolomite into ankerite. QA—quartz overgrowth; QD—detrital quartz; Fc—ferrocalcite; FD—feldspar dissolution; An—ankerite; Daw—dawsonite; AL—albite; Do—dolomite.

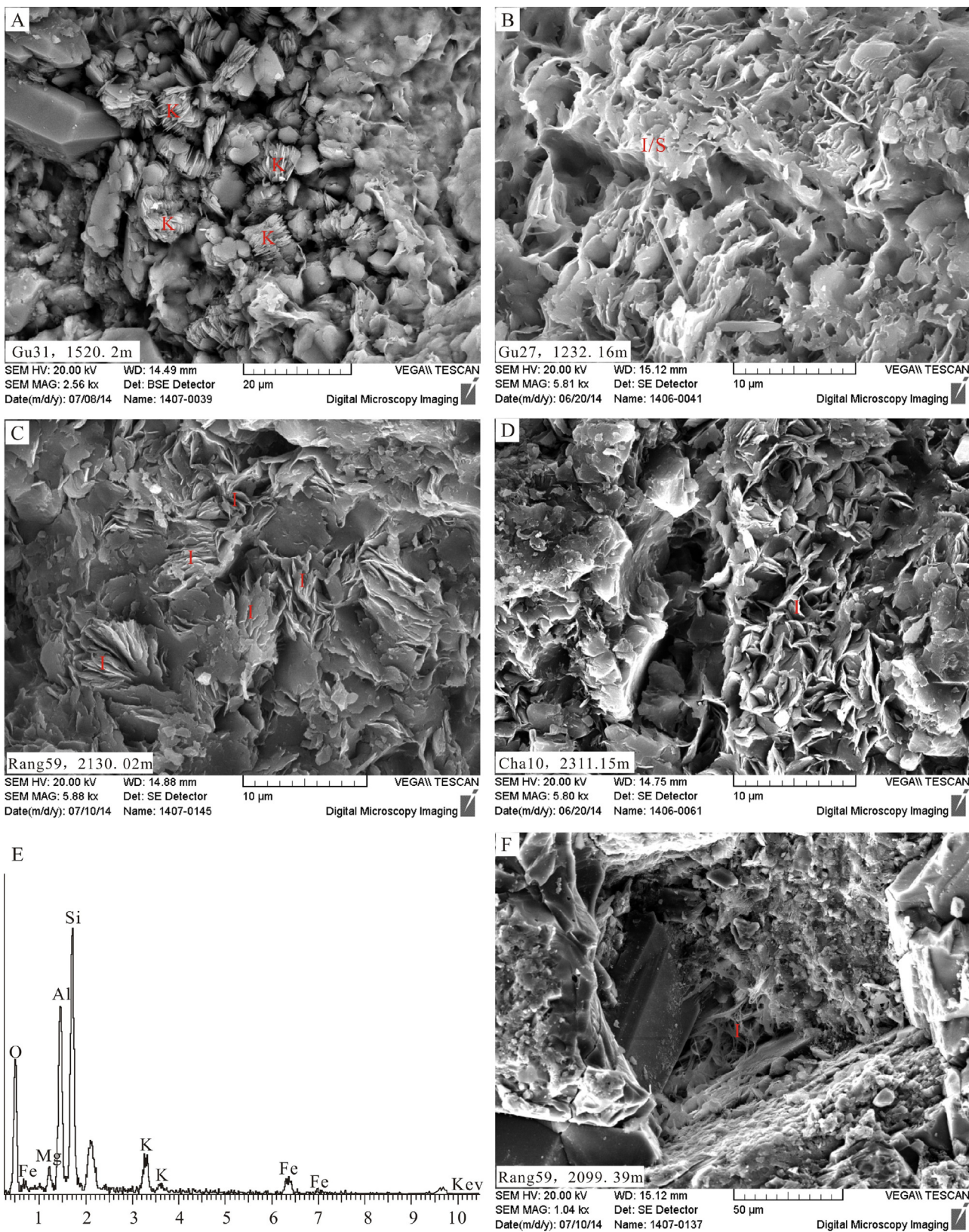


Fig. 8. Clay mineral characteristics in K₁q₄ sandstone reservoirs. (A) Micrograph of SEM showing kaolinite; (B) Micrograph of SEM showing mixed-layer I/S; (C and D) Micrographs of SEM showing flaky crystal illite. (E) The EDS showing FeMg-illite; (F) Micrographs of SEM showing fabric crystal illite. K—kaolinite; I/S—mixed-layer illite/smectite; I—illite.

revealed by SEM. Kaolinite, being a minor phase, occurs as vermicular stacked pseudohexagonal crystals (Fig. 8A). Mixed-layer illite/smectite with R=1 or R=3 are mainly present as foliated or

honeycomb fillings in primary porosity (Fig. 8B). Illite mainly exists in primary pores and sometimes on grain surface and in feldspar dissolution pores, occurring as flaky (Fig. 8C-E) and fibrous (Fig. 8F)

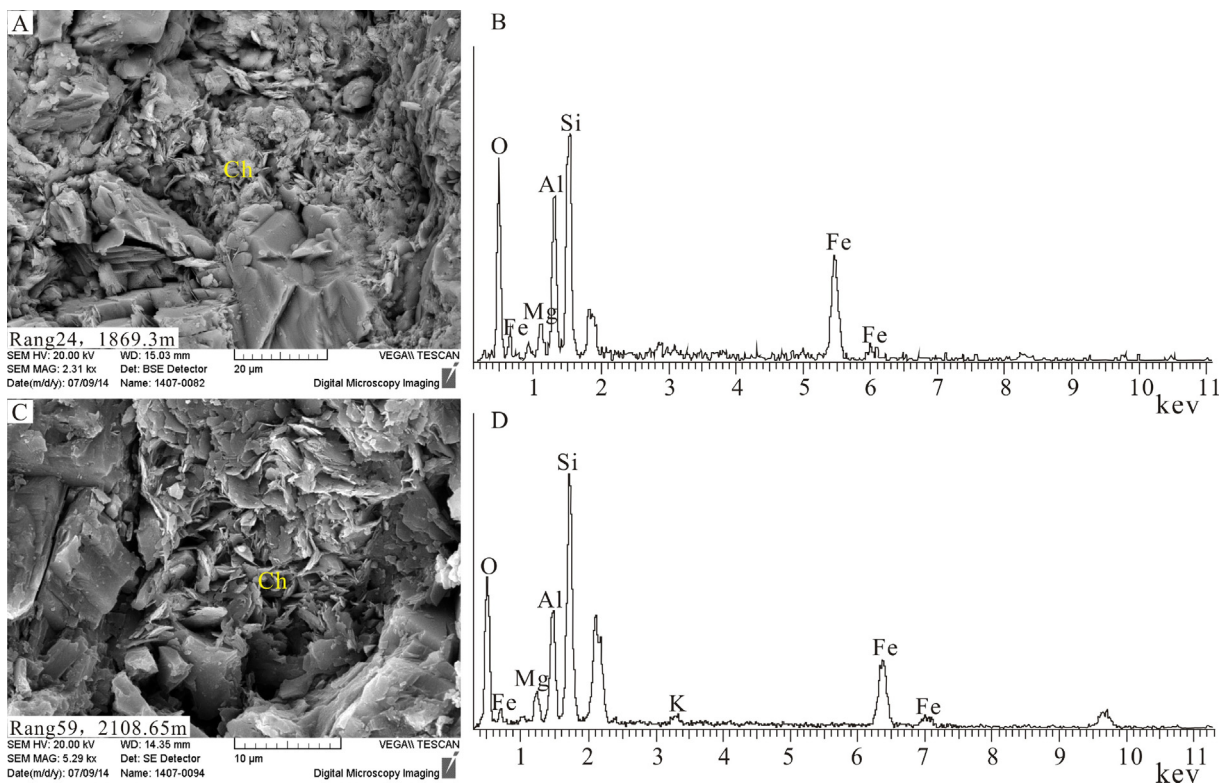


Fig. 9. The characteristics of chlorite in K₁ q₄ sandstone reservoirs. (A and C) Micrographs of SEM showing chlorite; (B and D) The EDS showing iron rich chlorite. Ch—chlorite.

crystals. Iron-rich chlorite mainly exists in the “pristine” sediments (Fig. 9A–D).

The fluid inclusions commonly present in the fractures on quartz grains, which may provide valuable information for continuous fluid activities in the sandstones during burial process (Robinson and Gluyas, 1992). Fluid inclusions were found in fractured quartz grains and ranged in size from about 2.3 μm to 9.16 μm . Most of the aqueous inclusions consist of two phases and have gas bubbles at room temperature. The homogenization temperature of the aqueous inclusions of the “pristine” sediments ranges from 73 to 117 $^{\circ}\text{C}$ with an average of 92.9 $^{\circ}\text{C}$. There were no data from the altered zones, but the homogenization temperature shows highest values along the sharp boundaries to the altered zones (Fig. 4).

Isotopic composition of carbonate cements was measured on 87 sandstone samples and 30 interbedded mudstones. The types and contents of carbonate cements in sandstone samples were identified by XRD and thin sections. In the “pristine” sediments, the $\delta^{13}\text{C}$ value (V-PDB) ranges from -12.2 to -2.9‰ with an average of -9.4‰ (mainly centered on -8.0 to -12.9‰), and $\delta^{18}\text{O}$ value (V-PDB) ranges from -22.9 to -18.2‰ with an average of -21.0‰ (Fig. 10, Table 7). In the CO₂ altered zones, $\delta^{13}\text{C}$ values (V-PDB) range from -9.2 to -0.9‰ with an average of -5.2‰ (mainly centered on -0.9 to -8.0‰), and $\delta^{18}\text{O}$ value (V-PDB) ranges from -21.7 to -18.2‰ with an average of -20.0‰ (Fig. 10, Table 8). The $\delta^{13}\text{C}$ value in the CO₂ altered zones was higher than that in the “pristine” sediments, while the $\delta^{18}\text{O}$ value looks similar (Fig. 10), indicating that the carbon source of the carbonate cements in the CO₂ altered zones was influenced by magmatic CO₂ (Worden, 2006; Gao et al., 2007; N. Liu et al., 2011). The wells that contained dawsonite mainly distribute along the deep-rooted faults (Fig. 11), which may also provide a good indication for an external magmatic CO₂ source and fluid mobilization. In interbedded mudstones, the $\delta^{13}\text{C}$ value (V-PDB) ranges from -13.3 to -0.9‰ with an average of -6.2‰, and $\delta^{18}\text{O}$ value (V-PDB) ranges from -21.7 to -12.1‰ with an average

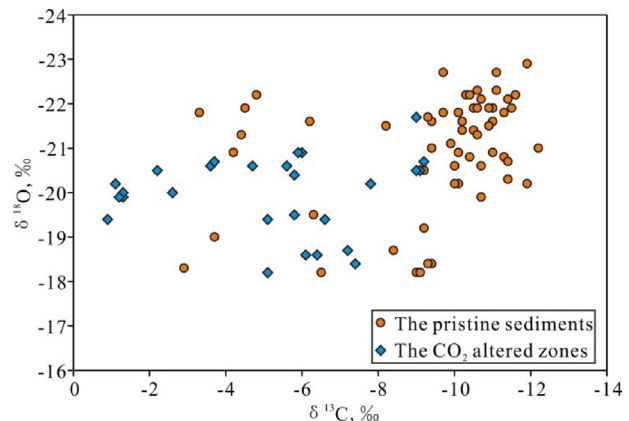


Fig. 10. The comparison of the carbon and oxygen isotope between the pristine sediments and CO₂ altered zones.

of -16.5‰ (Fig. 5). The obtained $\delta^{13}\text{C}$ and $\delta^{18}\text{O}$ values can be used to recognize the origin of the initial pore water indirectly. Marine carbonates are characterized with Z-value above 120, fresh-water types with Z-value below 120 and intermediate ones with Z-value near 120 (Keith and Weber, 1964). The calculation results show that the Z-value ranges from 91.52 to 115.8 with an average of 100.75 in sandstones (Tables 7 and 8) and from 90.90 to 122.33 with an average of 107.49 in interbedded mudstones. This indicates that the initial pore water was mainly fresh-water with very slight mixture of salt-water. It is expected that influx of low alkalinity hydrothermal fluids along the deep rooted fault facilitated rock-water interactions and hence released some alkali metal ions into the pore water and increased the salinity. When this hydrothermal solution reached to the dawsonite and ankerite zone, the reservoirs probably had the temperature from about 100 to 140 $^{\circ}\text{C}$ with an

Table 7

Mineralogical and isotopic composition of carbonate cements, and calculated Z-value in the “pristine” sediments.

Well	Depth, m	Carbonate minerals	$\delta^{13}\text{C}_{\text{PDB}}, \text{\textperthousand}$	$\delta^{18}\text{O}_{\text{PDB}}, \text{\textperthousand}$	Z value
Cha19	2282.45	100% Fc	-11.9	-20.2	92.87
Cha19	2284.35	60% Fc + 40% An	-9.4	-21.6	97.29
Cha19	2285.15	100% Fc	-8.2	-21.5	99.80
Hei160	2523.08	100% Fc	-4.2	-20.9	108.29
Hei160	2525.25	100% Fc	-4.4	-21.3	107.68
Hei160	2526.1	100% Fc	-4.5	-21.9	107.18
Hei160	2526.4	100% Fc	-4.8	-22.2	106.41
Hei160	2533.9	100% Fc	-10.6	-22.3	94.49
Rang24	1846.09	100% Fc	-11.1	-22.7	93.26
Rang24	1847.3	100% Fc	-9.3	-21.7	97.45
Rang24	1853.7	100% Fc	-10.3	-22.2	95.15
Rang24	1854	100% Fc	-10.5	-21.9	94.89
Rang24	1854.35	100% Fc	-10.4	-22.2	94.95
Rang24	1860.8	100% Fc	-10.1	-20.2	96.56
Rang24	1861.3	100% Fc	-11.3	-21.8	93.30
Rang24	1862.7	100% Fc	-11.9	-22.9	91.52
Rang24	1863.5	100% Fc	-10.7	-22.1	94.38
Rang24	1869.3	100% Fc	-9	-18.2	109.67
Rang24	1872.2	100% Fc	-9.9	-21.1	109.41
Rang24	1872.4	100% Fc	-6.3	-19.5	107.42
Rang24	1872.7	100% Fc	-9.7	-22.7	104.60
Rang24	1874.02	100% Fc	-10.2	-21.4	105.57
Rang24	1875.12	100% Fc	-6.5	-18.2	104.81
Rang24	1875.63	100% Fc	-9.4	-18.4	107.79
Rang24	1878.35	100% Fc	-11.4	-22.1	92.87
Rang59	2040.13	100% Fc	-3.3	-21.8	97.29
Rang59	2044.74	100% Fc	-3.7	-19	99.80
Rang59	2047.47	100% Fc	-2.9	-18.3	112.25
Rang59	2054.49	100% Fc	-6.2	-21.6	103.85
Rang59	2099.93	100% Fc	-10.5	-21.4	95.14
Rang59	2100.62	100% Fc	-10.7	-19.9	95.48
Rang59	2101.19	100% Fc	-11.6	-22.2	92.49
Rang59	2101.76	100% Fc	-11	-21.6	94.02
Rang59	2103.11	100% Fc	-11	-21.9	93.87
Rang59	2107.27	100% Fc	-10.2	-21.6	95.65
Rang59	2107.37	100% Fc	-11.5	-21.9	92.84
Rang59	2108.2	100% Fc	-10.4	-20.8	95.64
Rang59	2109.23	100% Fc	-10	-20.6	96.56
Rang59	2110	100% Fc	-10.1	-20.9	96.21
Rang59	2111.14	100% Fc	-10.1	-21.8	95.76
Rang59	2111.87	100% Fc	-9.4	-21	97.59
Rang59	2112.52	100% Fc	-11.1	-22.3	93.46
Rang59	2112.69	100% Fc	-10.6	-21.9	94.69
Rang59	2116.41	100% Fc	-9.3	-18.4	99.09
Rang59	2117.84	100% Fc	-10.7	-20.6	95.13
Rang59	2120.69	100% Fc	-9.2	-19.2	98.90
Rang59	2121.2	100% Fc	-10	-20.2	96.76
Rang59	2124.05	100% Fc	-9.1	-18.2	99.60
Rang59	2125.85	100% Fc	-10	-20.6	96.56
Rang59	2127.36	100% Fc	-8.4	-18.7	100.78
Rang59	2128.59	100% Fc	-10.9	-21.9	94.07
Rang59	2130.02	100% Fc	-9.7	-21.8	96.58
Xin125	1340	100% Fc	-9.2	-20.5	98.25
Xin125	1343	100% Fc	-10.9	-21.5	94.27
Xin125	1343.6	100% Fc	-11	-20.9	94.36
Xin125	1345.32	100% Fc	-10.6	-21.3	94.98
Xin125	1346.4	100% Fc	-11.4	-20.3	93.84
Xin125	1357.5	100% Fc	-11.3	-20.8	93.80
Xin125	1363.57	100% Fc	-11.4	-20.7	93.64
Xin125	1369	100% Fc	-12.2	-21	91.86

An—ankerite; Fc—ferrocalcite.

alkaline brine solution (N. Liu et al., 2011; Xi et al., 2015) (Fig. 12). The salinity of the pore water ranges from 8.02 g/L to 39.55 g/L with an average of 19.92 g/L in the CO₂ altered zones at present, while it shows a mean value of 9.92 g/L, varying from 7.28 g/L to 12.06 g/L in the “pristine” sediments. In addition, the δ¹³C, δ¹⁸O and Z-value all show sharp boundaries, where transition occurred from one domain to the other (Figs. 4 and 5).

4.4. Mass-balance constraints on the alteration reactions

The data sampled and analyzed in this study and also other studies in the same region (Gao et al., 2009; L. Liu et al., 2011; N. Liu et al., 2011) suggest that CO₂-rich magmatic fluids are responsible for the alteration of clay minerals and feldspars into carbonates such as ankerite (CaFe_{0.6}Mg_{0.4}(CO₃)₂) and dawsonite (NaAl(OH)₂CO₃). The alternative is that the CO₂ is locally sourced from carbonates and this is indeed observed by the conversion of dolomite into

Table 8

Mineralogical and isotopic composition of carbonate cements, and calculated Z-value in the CO₂ altered zones.

Well	Depth, m	Carbonate minerals	$\delta^{13}\text{C}_{\text{PDB}}, \text{\textperthousand}$	$\delta^{18}\text{O}_{\text{PDB}}, \text{\textperthousand}$	Z value
Cha10	2280.75	100% An	-3.6	-20.6	109.67
Cha10	2284.49	100% An	-3.7	-20.7	109.41
Cha10	2302	100% An	-4.7	-20.6	107.42
Cha10	2311.15	100% An	-6	-20.9	104.60
Cha10	2312.26	100% An	-5.6	-20.6	105.57
Cha10	2312.37	100% An	-5.9	-20.9	104.81
Cha10	2316.04	100% An	-5.1	-18.2	107.79
Cha21	2107.4	100% Fc	-5.8	-19.5	105.71
Cha21	2127.3	100% Fc	-9.1	-20.5	98.45
Cha21	2132.1	100% Fc	-9.2	-20.7	98.15
Cha21	2144	100% An	-5.8	-20.4	105.26
Cha21	2145.8	100% An	-1.1	-20.2	114.99
Cha21	2149.25	100% An	-9	-20.5	98.66
Gu27	1195.64	100% An	-2.2	-20.5	112.59
Gu27	1204.6	100% An	-0.9	-19.4	115.80
Gu27	1208.42	100% An	-1.3	-19.9	114.73
Gu27	1226.4	100% An	-2.6	-20	112.02
Gu27	1232.16	100% An	-1.3	-20	114.68
Gu27	1233.62	100% An	-1.2	-19.9	114.93
Gu31	1503.45	100% An	-5.1	-19.4	107.19
Gu31	1506.4	100% An	-7.2	-18.7	103.24
Gu31	1515.5	90% Fc + 10% An	-7.8	-20.2	101.27
Gu31	1518.1	100% An	-7.4	-18.4	102.98
Gu31	1519	100% An	-6.1	-18.6	105.54
Gu31	1520.2	85% Fc + 15% An	-6.6	-19.4	104.12
Gu31	1521.99	100% An	-6.4	-18.6	104.93
Gu31	1524.19	100% An	-9	-21.7	98.06

An—ankerite; Fc—ferrocalcite.

Table 9

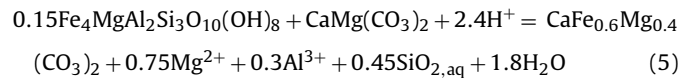
Table of rock composition for the modeling and changes in mass (moles) of minerals between the “pristine” and “altered” zones normalized to 1.0 L of pore space. Positive Δmol denotes growth whereas negative means dissolution.

Composition			Volume, %	Volume, %	Mw.	Dens., g/cm ³	mol/L (pore water)		
			“Pristine” rock norm.	CO ₂ -altered norm.			“Pristine” rock	“Altered”	Δmol
Silicates	Quartz	SiO ₂	48.65	48.21	60.08	2.65	246.77	244.55	-2.21
	K-feldspar	KAlSi ₃ O ₈	5.81	3.00	278.22	2.56	6.14	3.17	-2.97
	Plagioclase	Ca _{0.2} Na _{0.8} Al _{1.2} Si _{2.8} O ₈	24.62	17.58	265.41	2.65	28.27	20.19	-8.08
	Chlorite	Fe ₄ MgAl ₂ Si ₃ O ₁₀ (OH) ₈	5.21	0.29	681.97	3.13	2.75	0.15	-2.59
	Illite	KMg _{0.27} Fe _{0.3} Al _{1.53} Al _{0.73} Si _{3.27} O ₁₀ (OH) ₂	9.41	18.84	409.13	2.75	7.27	14.56	7.29
	Kaolinite	Al ₂ Si ₂ O ₅ (OH) ₄	0.40	0.87	258.16	2.62	0.47	1.01	0.55
Carbonates	Calcite	CaCO ₃	5.91	1.55	100.09	2.71	18.39	4.81	-13.58
	Ankerite	CaFe _{0.6} Mg _{0.4} (CO ₃) ₂	0.00	5.80	203.33	3.05	0.00	10.00	10.00
	Dawsonite	NaAl(OH) ₂ CO ₃	0.00	3.86	144.00	2.42	0.00	7.47	7.47

ankerite (Fig. 7M–O). The formation of the secondary carbonates furthermore indicates supply of Fe, Mg, Ca (ankerite), and Na and Al (dawsonite). This may be from dissolving plagioclase (Ca, Al, and Na), and chlorite (Fe, Al and possibly Mg), both indicated to have dissolved locally. Dawsonite is found to correlate negatively with plagioclase and kaolinite (Fig. 13A), indicating that these two may be aluminium sources for the dawsonite growth. Furthermore, the chlorite is observed to disappear in the intervals where ankerite is abundant (Fig. 13B). In order to prepare a reactive assemblage for the kinetic modeling we first performed a simple inverse modeling. Table 9 provides the moles of each mineral present in the “pristine” and altered parts of the sediment, normalized to one liter pore water and assuming that the porosity is 8% in both sediments. We then assume that all iron for ankerite growth must have come from the chlorite, and all sodium for dawsonite must have come from the plagioclase. This provides rough estimates because of the uncertainty in the quantitative XRD, but still serves as valuable input to the kinetic modeling.

Table 9 indicates that about 10.0 mol of ankerite have formed per liter pore space. It was difficult to distinguish dolomite from ankerite and part of the 10 mol is assumed to be primary dolomite

(Fig. 7M–O). Petrographic examinations suggest that the dolomite had been partly replaced by ankerite (Fig. 7M–O), and we therefore assume that the ankerite formed from a conversion of dolomite in the presence of Fe²⁺ sourced from chlorite:



Eq. (5) suggests that 0.15 mol of chlorite is required per mole of ankerite formed, whereas Mg, Si and Al are released in the reaction. The total amount of chlorite that dissolved was about 2.6 mol, more than sufficient to explain the complete conversion of dolomite to ankerite, suggesting that another sink for Mg and Fe must have been present to drive the chlorite dissolution. Our data suggests that kaolinite and K-feldspar has reacted to form illite in the altered zone, and illite may be the sink for both Fe and Mg. According to the SEM-EDS, the illite is aluminium-rich and containing roughly equal amount of Mg and Fe (Fig. 8C–F), and illite was therefore modeled as an ideal solid-solution between muscovite (KAl₃Si₃O₁₀(OH)₂), annite (KFe₃AlSi₃O₁₀(OH)₂), and celadonite (KMgAlSi₄O₁₀(OH)₂). The conversion of the K-feldspar and kaolinite to illite, with excess

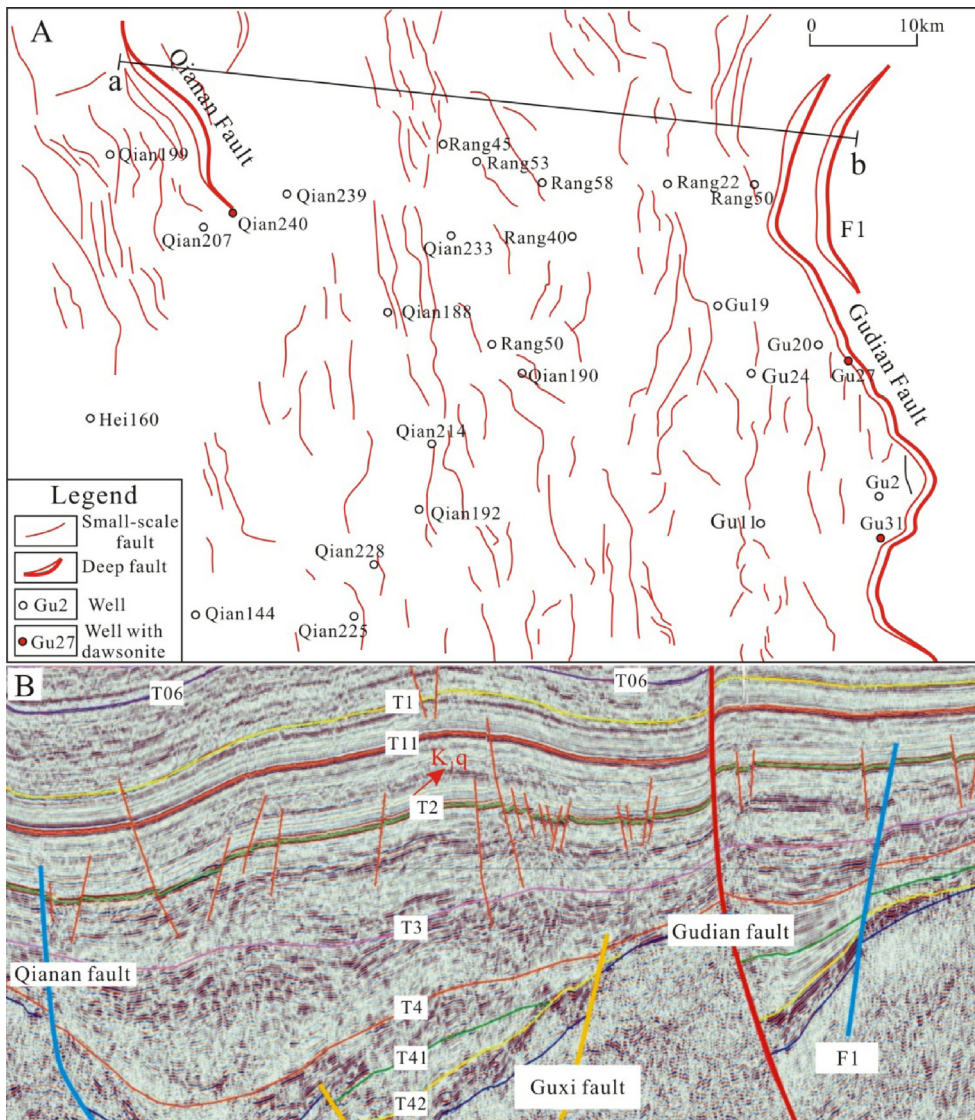
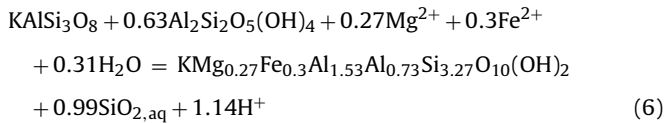
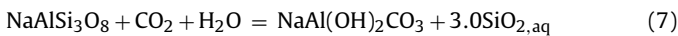


Fig. 11. The top structure map of K₁q₄ and seismic profile (modified from Lu et al., 2011) showed that the well with dawsonite mainly distribute along the deep rooted faults. The transect (a–b) in the upper map just shows the approximate position of the lower seismic profile.

Fe and Mg, can then be written as:



The XRD data and SEM observations (Fig. 7J–L) suggested that plagioclase has dissolved and have been replaced by dawsonite. Table 9 indicates that about 7.5 mol of dawsonite have formed per liter pore space. The CO₂ source for dawsonite may have been CO₂ supplied in an open-system hydrothermal system, or local dissolution from a carbonate, such as calcite. A local calcite as CO₂ source would lead to increased aqueous Ca²⁺, and would require an additional Ca-sink. Such a sink has not been observed and we therefore wrote the plagioclase to dawsonite reaction using aqueous CO₂ as carbonate source. We here used the albite (NaAlSi₃O₈) plagioclase end-member to illustrate the conversion reaction:



From Eq. (7) we see that it is a 1:1 relation between amount of albite dissolving and dawsonite forming. The XRD data suggest that about 8.1 mol of plagioclase dissolved (Table 9), being close to the 7.5 mol of dawsonite formed.

There is a net release of Al and Si from Reactions (5) and (7), and these two elements may combine to form kaolinite, quartz, and smectite. The kaolinite could then be consumed in the conversion of K-feldspar to illite (Reaction (6)) if excess K-feldspar was present. The above mass balances support that Reactions (5) and (7) are the main mineral reactions storing CO₂. Because aluminium is conserved in the conversion of kaolinite and K-feldspar to illite, dawsonite is not likely to be sourced from K-feldspar (Hellevang et al., 2011, 2014).

4.5. Kinetic modeling of the CO₂-induced alteration

The input amounts of minerals in the pristine rocks was based on the XRD% and recalculated to moles per liter formation water (Table 9). The amount of secondary ankerite listed in this table is too high since it was difficult to separate secondary ankerite from the primary dolomite. In the kinetic modeling we therefore added

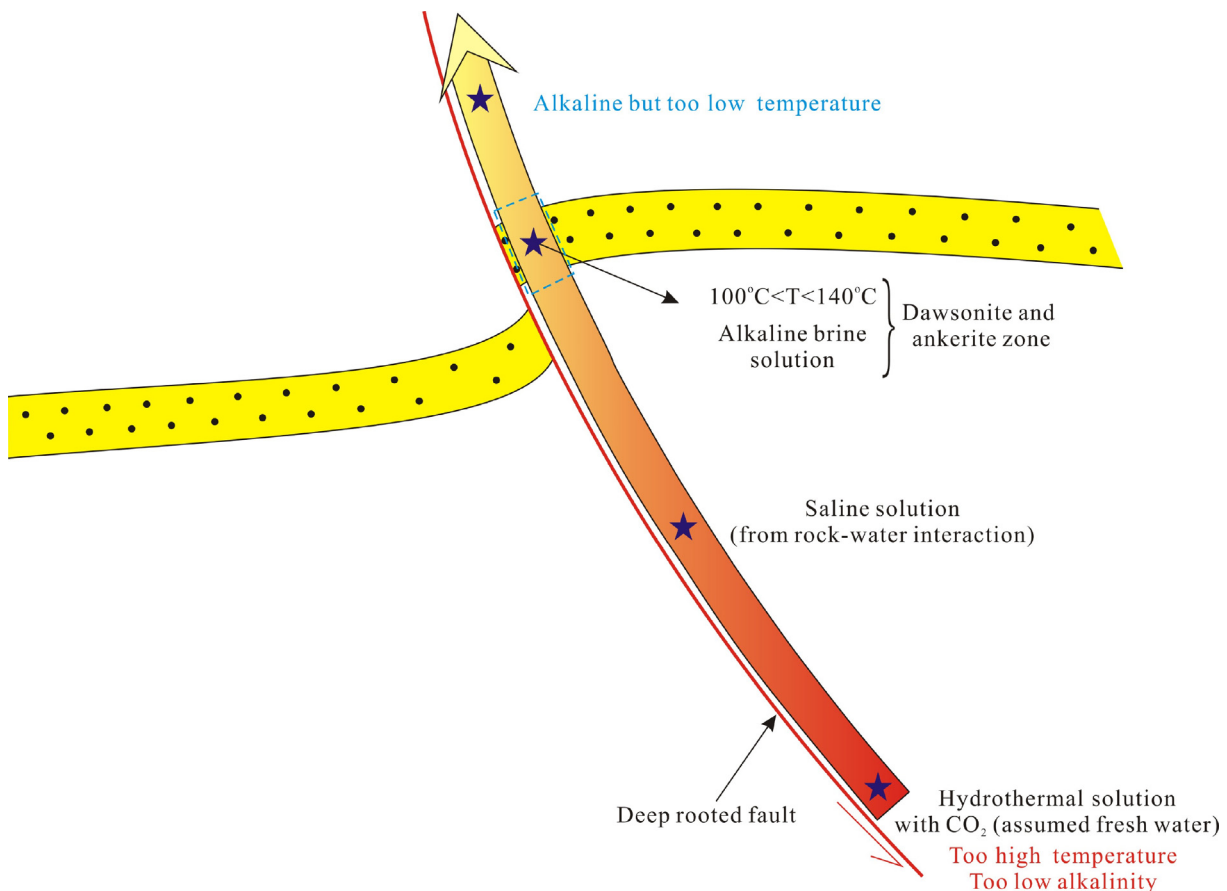


Fig. 12. The conceptual sketch showing the hydrothermal solution evolution from source to the reservoirs with alteration products dawsonite and ankerite.

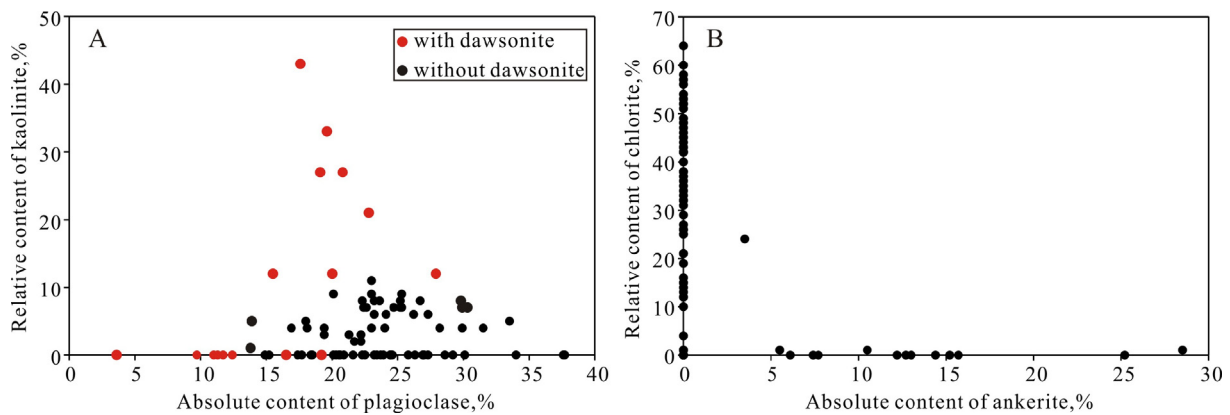


Fig. 13. The plots show the dissolution of plagioclase and chlorite. (A) The relationship between absolute content of plagioclase and relative content of kaolinite; (B) the relationship between absolute content of ankerite and relative content of chlorite.

five moles of dolomite per liter formation water (half that of the estimated ankerite) to the initial mineral assemblage.

The first step of the kinetic simulations was to estimate reactive surface areas giving the observed changes in chlorite and plagioclase. This was done by trial and failure until the simulated changes were close to the observed. Using the surface area as estimated in the Methods section (Equation (2) with $r_{\varphi} = 144$, $\xi_{\text{plag}} = 0.1$ and $\xi_{\text{chl}} = 10$, and with $\alpha = 1$) provides reasonable results, but the amount of plagioclase dissolving is too large, and the amount of kaolinite, ankerite and dawsonite is also too large (Fig. 14a). If α is reduced to 0.2, the feldspar dissolution can be predicted well, and also the amounts of dawsonite and ankerite is close to the observed

(Fig. 14b). This suggests that laboratory kinetic parameters from Palandri and Kharaka (2004) in combination with the reactive surface area model as defined by Hellevang and Aagaard (2013) (based on the pore geometry rather than normalized to mass) works well for the low-porosity ($\sim 8\%$) natural system. If a mass-normalized model was used, the estimated reactive surface area would be orders of magnitude larger and the predicted rates would be correspondingly orders of magnitude too fast (or the fraction of the surface being reactive would be unreasonable low) (Hellevang and Aagaard, 2013).

Despite indications of hydrothermal and CO_2 -induced alteration (formation of fibrous illite, ankerite and dawsonite), there is no

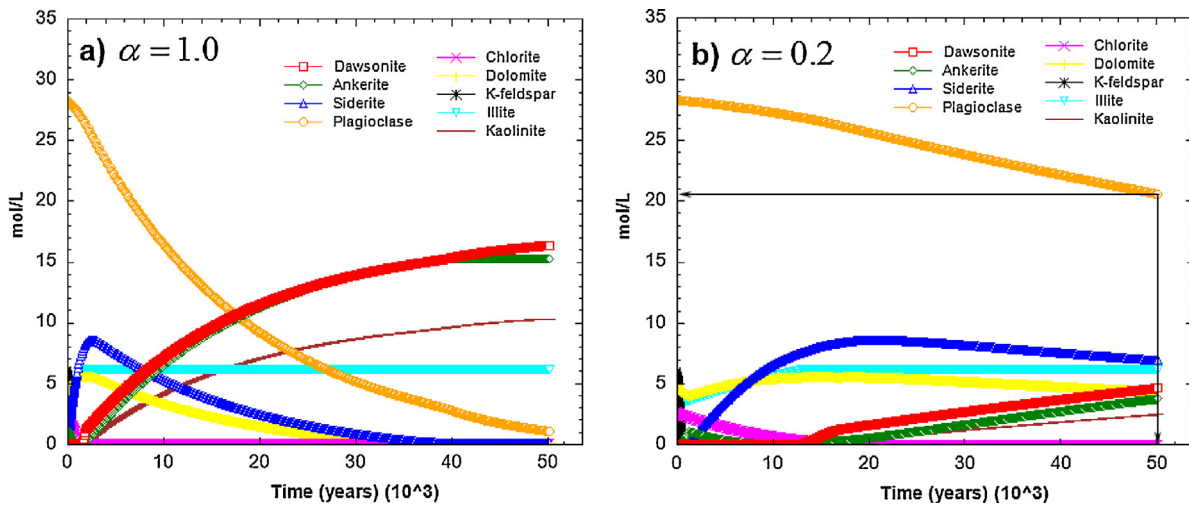


Fig. 14. Tuning the α parameter for the reactive surface area (Eq. (2)) to the observed plagioclase dissolution (~ 20.5 mol/L porespace left in the altered zone). Assuming a time span of 50,000 years of rock alteration gives an $\alpha = 0.2$ ($r_\varphi = 144$, $\xi_{\text{plag}} = 0.1$ and $\xi_{\text{chl}} = 10$).

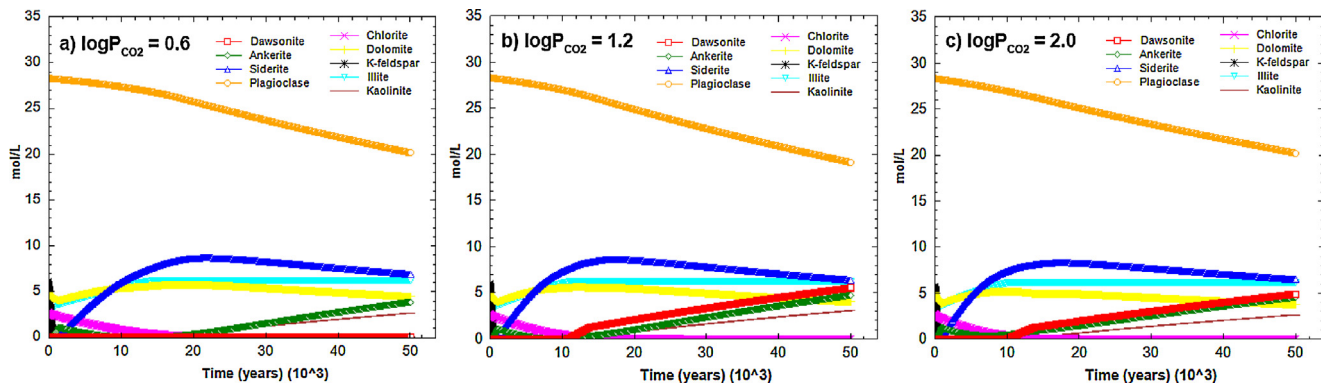


Fig. 15. Simulated alteration of the Quantou Fm. at 120 °C and varying the partial pressure of CO₂ from 1 to 100 bar, and using labradorite (An40) to represent the plagioclase feldspar.

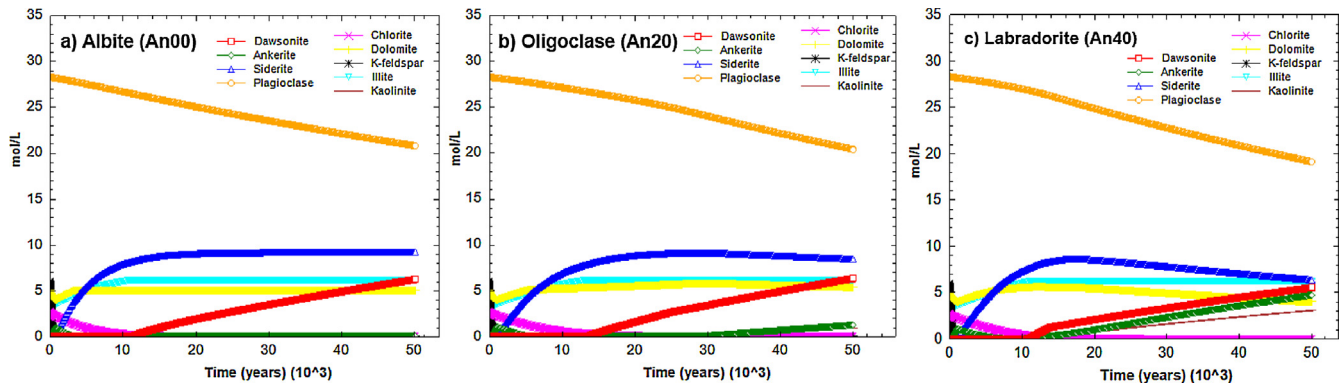


Fig. 16. Simulated alteration of the Quantou Fm. at 120 °C and a CO₂ partial pressure of ~ 16 bar and with varying plagioclase compositions from pure albite (a) to labradorite (c).

data on the partial pressure of CO₂ during the alteration, and the temperature is also uncertain. The composition of the plagioclase dissolving to form dawsonite is also not known. We therefore performed a comprehensive set of simulations varying CO₂ pressure, temperature and plagioclase composition (Albite to Labradorite (An40)). All simulations were done over a timeframe of 50,000 years, and α was adjusted for each simulation to obtain extents of plagioclase dissolution close to the observed. The results are provided in Supplementary Figs. S1–S3. Some of the simulations

have been selected here to illustrate the main findings. It is clear from these simulations that the CO₂ partial pressure must have been higher than 1.0 bar. No dawsonite formed at the low CO₂ partial pressure and for all temperatures and plagioclase compositions. At ~ 16 bar or higher, both ankerite and dawsonite are indicated to form and there is not much difference between 16 and 100 bar (Fig. 15). It is furthermore concluded that the pure albite end-member cannot reproduce the observed mineral changes as ankerite is lacking or is formed in very small amounts. The amount

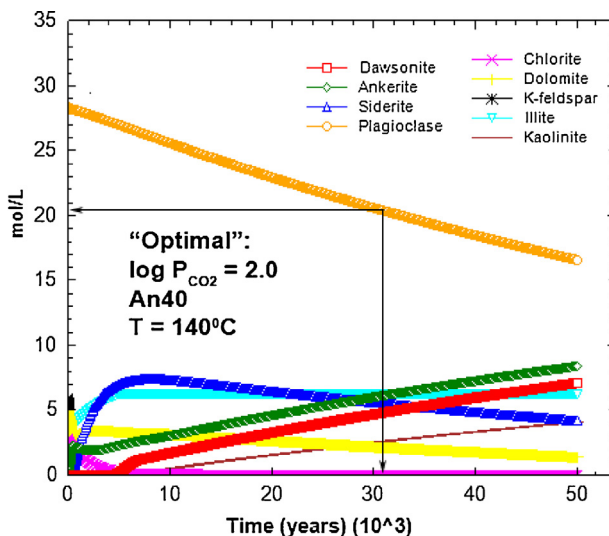


Fig. 17. Based on all simulations (Supplementary Figs. S1–S3) the simulated alteration patterns being closest to XRD data were obtained at 140 °C, a partial CO₂ pressure of 100 bar, and using the most calcic plagioclase labradorite.

of ankerite increases proportionally to Ca content of the plagioclase, and the most calcic plagioclase generates most ankerite and with an amount being similar but somewhat less than the observed (Fig. 16). The explanation for this is that extra supply of calcium is a driver for stabilizing ankerite relative to siderite and dolomite, driving the dissolution of the chlorite forward, which is in turn providing excess Al supply for dawsonite growth. The relative amounts of ankerite and dawsonite also depend on temperature, with ankerite increasing with temperature. The closest match between simulated and observed alteration is therefore found for the most calcic plagioclase (Labradorite), at the highest CO₂ pressure (100 bar) and at the highest temperature 140 °C (Fig. 17). Increasing the Ca content of the plagioclase further would lead to even more ankerite in the expense of siderite and probably even closer match to the observed changes. We did not have a thermodynamic stability of An60, and did therefore not attempt such a simulation.

5. Conclusions

The sandstones of the Quantou Fm. in the Songliao Basin can be divided into two distinct zones based on their mineralogy. One part is dominated by quartz, plagioclase, and chlorite, and with only calcite and dolomite belonging to the carbonate mineral group. The second part is still dominated by quartz, but contains abundant secondary illite, illite/smectite and chlorite is absence. Ankerite and dawsonite are the dominant carbonates in the altered zone. The ankerite/dawsonite and clay-bearing zones have been found related to the major deep-rooted faults in this area. We therefore proposed that these zones have experienced hydrothermal (~100–140 °C) alteration and with a similar precursor mineral assemblage as in the plagioclase/chlorite rich zones. Based on this we named the zones “pristine” and “altered”. To test if this could indeed be the case we performed a simple inverse estimate of the mole transfers, based on quantitative XRD measurements. We found that the most likely source of ankerite was a precursor dolomite and with chlorite dissolution supplying iron. The dawsonite formation could be explained well with a corresponding dissolution of the plagioclase. It was concluded from this part that an external source of CO₂ is needed to explain the dawsonite formation. Based on the inverse estimates we furthermore performed kinetic/thermodynamic modeling to see if the hydrothermal CO₂

charged solutions could explain the observed alteration patterns. The main findings from these simulations are:

- The general alteration patterns, the replacement of dolomite and chlorite by ankerite, plagioclase by dawsonite, and the formation of mainly FeMg-illite rather than kaolinite, is predicted using a closed-system model with a constant high CO₂ pressure. The best fit between model and observations was found at the highest temperature and highest CO₂ partial pressure (100 atm), and using the most calcic plagioclase as source for the dawsonite. Too low CO₂ pressures stabilize chlorite and prevent the dolomite to ankerite transformation.
- A good match between model and observations was found using 50,000 years simulation with a pore surface-area normalization. Using such surface-area normalization for low-porosity rocks, rather than the ‘normal’ mass-normalized surface areas, may provide more realistic simulations of natural systems and may be of value also in the ongoing debate on the difference between natural and laboratory alteration kinetics.

Acknowledgements

This work has been partially funded by the National Natural Science Foundation of China (Grant No. U1262203), the Fundamental Research Funds for the Central Universities (Grant No. 15CX08001A and 15CX05007A), the Chinese Scholarship Council (No. 201406450019), and FME SUCCESS center for CO₂ storage under grant 193825/S60 from Research Council of Norway (RCN). FME SUCCESS is a consortium with partners from industry and science, hosted by Christian Michelsen Research AS. Engineers Desheng Zhu and Jianchang You at the Research Institute of Petroleum Exploration & Development are thanked for SEM, XRD analysis. We also thank the Jilin Oil field, PetroChina, for providing data.

Appendix A. Supplementary data

Supplementary data associated with this article can be found, in the online version, at <http://dx.doi.org/10.1016/j.ijggc.2016.07.010>.

References

- Aagaard, P., Helgeson, H.C., 1982. Thermodynamic and kinetic constraints on reaction rates among minerals and aqueous solutions; I, theoretical considerations. *Am. J. Sci.* 282, 237–285.
- Barclay, S.A., Worden, R.H., 2000. Geochemical modelling of diagenetic reactions in a sub-arkosic sandstone. *Clay Miner.* 35, 57–67.
- Benson, S.M., Cole, D.R., 2008. CO₂ sequestration in deep sedimentary formations. *Elements* 4, 325–331.
- Bjørlykke, K., Egeberg, P.K., 1993. Quartz cementation in sedimentary basins. *AAPG Bull.* 77, 1538–1548.
- Bjørlykke, K., Jahren, J., 2012. Open or closed geochemical systems during diagenesis in sedimentary basins: constraints on mass transfer during diagenesis and the prediction of porosity in sandstone and carbonate reservoirs. *AAPG Bull.* 96, 2193–2214.
- Duan, Z., Sun, R., 2003. An improved model calculating CO₂ solubility in pure water and aqueous NaCl solutions from 273 to 533 K and from 0 to 2000 bar. *Chem. Geol.* 193, 257–271.
- Farquhar, S.M., Pearce, J.K., Dawson, G.K.W., Golab, A., Sommacal, S., Kirste, D., Biddle, D., Golding, S.D., 2015. A fresh approach to investigating CO₂ storage: experimental CO₂–water–rock interactions in a low-salinity reservoir system. *Chem. Geol.* 399, 98–122.
- Folk, R.L., 1974. *Petrology of Sedimentary Rocks*. Hemphill, Austin, Texas, pp. 182.
- Gao, Y., Liu, L., Yang, H., You, L., Liu, N., 2007. Characteristics and origin of dawsonite in Gudian carbon dioxide gas field of Songliao Basin. *Acta Petrolei Sin.* 28, 62–67.
- Gao, Y., Liu, L., Hu, W., 2009. Petrology and isotopic geochemistry of dawsonite-bearing sandstones in Hailaer basin, northeastern China. *Appl. Geochem.* 24, 1724–1738.
- Golab, A.N., Carr, P.F., Palamara, D.R., 2006. Influence of localised igneous activity on cleat dawsonite formation in Late Permian coal measures, Upper Hunter Valley, Australia. *Int. J. Coal Geol.* 66, 296–304.

- Gysi, A.P., Stefánsson, A., 2011. CO₂–water–basalt interaction. Numerical simulation of low temperature CO₂ sequestration into basalts. *Geochim. Cosmochim. Acta* 75, 4728–4751.
- Helgeson, H.C., 1967. Thermodynamics of complex dissociation in aqueous solution at elevated temperatures. *J. Phys. Chem.* 71, 3121–3136.
- Hellevang, H., Aagaard, P., 2013. Can the long-term potential for carbonatization and safe long-term storage in sedimentary formations be predicted? *Appl. Geochem.* 39, 108–118.
- Hellevang, H., Kvamme, B., 2006. ACCRETE-geochemistry solver for CO₂–waterrock interactions. In: *Proceedings of the GHGT8 Conference*, Trondheim, Norway, June 19–22, pp. 1–6.
- Hellevang, H., Declercq, J., Aagaard, P., 2011. Why is dawsonite absent in CO₂ charged reservoirs? *Oil Gas Sci. Technol.: Rev. IFP Energies Nouvelles* 66, 119–135.
- Hellevang, H., Aagaard, P., Jahren, J., 2014. Will dawsonite form during CO₂ storage? *Greenh. Gases Sci. Technol.* 4, 191–199.
- Hillier, S., 2003. Quantitative analysis of clay and other minerals in sandstones by X-ray powder diffraction (XRPD). In: Worden, R., Morad, S. (Eds.), *Clay Mineral Cements in Sandstones*. International Association of Sedimentologists, Special Publication, Oxford, pp. 213–251.
- Keith, L.M., Weber, N.J., 1964. Carbon and oxygen isotopic composition of selected limestones and fossils. *Geochim. Cosmochim. Acta* 28, 1787–1816.
- Liu, L., Hou, Q., Liu, N., Yang, H., Li, F., Yu, Z., 2011. Charging time sequence of mantle CO₂ and hydrocarbon in southern Songliao Basin: an evidence from dawsonite-bearing sandstones. *Oil Gas Geol.* 32, 873–881.
- Li, D., Dong, C., Lin, C., Ren, L., Jiang, T., Tang, Z., 2013. Control factors on tight sandstone reservoirs below source rocks in the Rangzijing slope zone of southern Songliao Basin, East China. *Petrol. Explor. Dev.* 40, 692–700.
- Liu, J., 2004. The simulation of thermal history in Changling Sag. *Nat. Gas Ind.* 24, 17–20.
- Lu, X., Wei, L., Song, Y., Liu, S., Fu, X., 2011. Study on the pool-forming mechanism of high content CO₂ gas pools in Changling fault-depression, south Songliao Basin. *Nat. Gas Geosci.* 22, 657–663.
- Lynch, L.F., Mack, E.L., Land, S.L., 1997. Burial diagenesis of illite/smectite in shales and the origins of authigenic quartz and secondary porosity in sandstones. *Geochim. Cosmochim. Acta* 61, 1995–2006.
- Mathias, S.A., Gluyas, J.G., Mackay, E.J., Goldthorpe, W.H., 2013. A statistical analysis of well production rates from UK oil and gas fields—implications for carbon capture and storage. *Int. J. Greenh. Gas Control* 19, 510–518.
- Metwally, M.Y., Chesnokov, M.E., 2012. Clay mineral transformation as a major source for authigenic quartz in thermo-mature gas shale. *Appl. Clay Sci.* 55, 138–150.
- Moore, D.M., Reynolds, R.C., 1997. *X-Ray Diffraction and the Identification and Analysis of Clay Minerals*. Oxford University Press, Oxford.
- Liu, N., Liu, L., Qu, X., Yang, H., Wang, L., Zhao, S., 2011. Genesis of authigenic carbonate minerals in the Upper Cretaceous reservoir, Honggang Anticline, Songliao Basin: a natural analog for mineral trapping of natural CO₂ storage. *Sediment. Geol.* 237, 166–178.
- Nordstrom, D.K., Plummer, L.N., Wigley, T.M.L., Wolery, T.J., Ball, J.W., Jenne, E.A., Bassett, R.L., Crerar, D.A., Florence, T.M., Fritz, B., Hoffman, M., Holdren, G.R., Lafon, G.M., Mattigod, S.V., McDuff, R.E., Morel, E., Reddy, M.M., Sposito, G., Thailkill, J., 1979. A comparison of computerized chemical models for equilibrium calculations aqueous systems. In: Jenne, E.A. (Ed.), *Chemical Modeling in Aqueous Systems*. ACS Symp. Series 93. Am. Chem. Soc.
- Palandri, J.L., Kharaka, Yousif K., 2004. A Compilation of Rate Parameters of Water-mineral Interaction Kinetics for Application to Geochemical Modeling, DTIC Document. Menlo Park, California.
- Parkhurst, D.L., Appelo, C.A.J., 2013. Description of Input and Examples for PHREEQC Version 3—A Computer Program for Speciation, Batch-Reaction, One-Dimensional Transport, and Inverse Geochemical Calculations. U.S. Geological Survey Techniques and Methods Report, Book 6, p. 497. Available from: <http://pubs.usgs.gov/tm/06/a43/> (Chapter A43).
- Pearce, J.K., Law, A.C.K., Dawson, G.K.W., Golding, S.D., 2015a. SO₂–CO₂ and pure CO₂ reactivity of ferroan carbonates at carbon storage conditions. *Chem. Geol.* 411, 112–124.
- Pearce, J.K., Kirste, D.M., Dawson, G.K.W., Farquhar, S.M., Biddle, D., Golding, S.D., Rudolph, V., 2015b. SO₂ impurity impacts on experimental and simulated CO₂–water–reservoir rock reactions at carbon storage conditions. *Chem. Geol.* 399, 65–86.
- Peltonen, C., Marcussen, Ø., Bjørlykke, K., Jahren, J., 2009. Clay mineral diagenesis and quartz cementation in mudstones: the effects of smectite to illite reaction on rock properties. *Mar. Petrol. Geol.* 26, 887–898.
- Robinson, A., Gluyas, J., 1992. Duration of quartz cementation in sandstones, North Sea and Haltenbanken Basins. *Mar. Petrol. Geol.* 9, 324–327.
- Rochelle, C.A., Cernichowski-Lauriol, I., Mlodowski, A.E., 2004. The Impact of Chemical Reaction on CO₂ Storage in Geological Formations: A Brief Review, vol. 233. *Geology Society London Special Publication*, pp. 87–106.
- Soave, G., 1972. Equilibrium constants from a modified Redlich–Kwong equation of state. *Chem. Eng. Sci.* 27, 1197–1203.
- Wilkinson, M., Haszeldine, R.S., 2002. Fibrous illite in oilfield sandstones—a nucleation kinetic theory of growth. *Terra Nova* 14, 56–60.
- Worden, R.H., Barclay, S.A., 2000. Internally-sourced quartz cement due to externally-derived CO₂ in sub-arkosic sandstones, North Sea. *J. Geochim. Explor.* 69–70, 645–649.
- Worden, R.H., Benshatwan, M.S., Potts, G.J., Elgarmadi, S.M., 2015. Basin-scale fluid movement patterns revealed by veins: Wessex Basin, UK. *Geofluids*, 1–26.
- Worden, R.H., 2006. Dawsonite cement in the Triassic Lam Formation, Shabwa Basin, Yemen: a natural analogue for a potential mineral product of subsurface CO₂ storage for greenhouse gas reduction. *Mar. Petrol. Geol.* 23, 61–77.
- Xi, K., Cao, Y., Jaren, J., Zhu, R., Bjørlykke, K., Zhang, X., Cai, L., Hellevang, H., 2015. Quartz cement and its origin in tight sandstone reservoirs of the Cretaceous Quantou formation in the southern Songliao basin, China. *Mar. Petrol. Geol.* 66, 748–763.
- Zhang, X., Zhang, L., 2013. Quantitive research on effective source rocks of the Denglouku formation in northern Songliao Basin. *Chin. J. Geol.* 48, 879–890.
- Zhang, W., Li, Y., Xu, T., Cheng, H., Zheng, Y., Xiong, P., 2009. Long-term variations of CO₂ trapped in different mechanisms in deep saline formations: a case study of the Songliao Basin, China. *Int. J. Greenh. Gas Control* 3, 161–180.
- Zhou, Z., Feng, D., Wang, H., Zhou, H., Wang, Q., 2012. Sequence stratigraphy framework of Qing 1 and Qing 2 members in the western slope of southern Songliao Basin and its control effect on reservoir sand bodies. *Lithol. Reserv.* 24, 39–50.
- Zou, C., Jia, C., Zhao, W., Tao, S., Gu, Z., Hou, J., Song, L., 2005. Accumulation dynamics and distribution of litho stratigraphic reservoirs in South Songliao Basin. *Petrol. Explor. Dev.* 32, 125–130.